Systems Analysis of Immune Changes after B-cell Depletion in Autoimmune Multiple Sclerosis

Jessica Wei[1,2]*, Jeonghyeon Moon[1,2]*, Yoshiaki Yasumizu[1,2,3], Le Zhang[1], Khadir Radassi[1], Nicholas Buitrago-Pocasangre[1], M. Elizabeth Deerhake[1], Nicolas Strauli[4], Chun-Wei Chen[4], Ann Herman[4], Rosetta Pedotti[5], Catarina Raposo[5], Isaiah Yim[6], Jenna Pappalardo[1,2], Erin E. Longbrake[1], Tomokazu S. Sumida[1], Pierre-Paul Axisa[1,2,7#†], David A. Hafler[1,2,8#†]

Affiliations

1. Department of Neurology, Yale School of Medicine, New Haven, CT, USA
2. Department of Immunobiology, Yale School of Medicine, New Haven, CT, USA
3. Department of Experimental Immunology, Immunology Frontier Research Center, Osaka University, Suita, Osaka, Japan
4. Genentech, San Francisco, CA
5. Roche, Basel, Switzerland
6. Department of Biomedical Engineering, Yale University, New Haven, CT, USA
7. Centre de recherches en cancérologie de Toulouse (CRCT), Inserm, Toulouse, France
8. Broad Institute, Boston, MA, USA

* equal contribution

# equal contribution

† correspondence: pierre-paul.axisa@inserm.fr and david.hafler@yale.edu

Abstract

Multiple sclerosis (MS) is a complex genetically mediated autoimmune disease of the central nervous system where anti-CD20-mediated B cell depletion is remarkably effective in the treatment of early disease. While previous studies investigated the effect of B cell depletion on select immune cell subsets using flow cytometry-based methods, the therapeutic impact on patient immune landscape is unknown. In this study, we explored how a therapy-driven "*in vivo perturbation*" modulates the diverse immune landscape by measuring transcriptomic granularity with single-cell RNA sequencing (scRNAseq). We demonstrate that B cell depletion leads to cell type-specific changes in the abundance and function of CSF macrophages and peripheral blood monocytes. Specifically, a CSF-specific macrophage population with an anti-inflammatory transcriptomic signature and peripheral $CD16^+$ monocytes increased in frequency post-B cell depletion. This was accompanied by increases in TNFα messenger RNA and protein in monocytes post-B cell depletion, consistent with the finding that anti-TNFα treatment exacerbates autoimmune activity in MS. In parallel, B cell depletion induced changes in peripheral $CD4^+$ T cell populations, including increases in the frequency of $TIGIT^+$ regulatory T cells and marked decreases in the frequency of myelin peptide loaded-tetramer binding $CD4^+$ T cells. Collectively, this study provides an exhaustive transcriptomic map of immunological changes, revealing different mechanisms of action contributing to the high efficacy in B cell depletion treatment of MS.

Introduction

While B cell depletion is efficacious in the treatment of various autoimmune diseases including rheumatoid arthritis and type 1 diabetes[1,2], it has conferred remarkable therapeutic benefits in early relapsing remitting multiple sclerosis (MS)[3]. While presumably pathogenic myelin-reactive T cells[4,5] with loss of regulatory T cell (Treg) function[6-8] have been established as mechanistic drivers of MS pathogenesis, accumulating evidence directly implicates B cells as key contributors to loss of immune tolerance. The central role of B cells in MS pathophysiology is substantiated by the infiltration of B cells into MS lesions and CSF[9], the presence of ectopic meningeal B cell follicles adjacent to areas of focal cortical demyelination[10,11], and the detection of oligoclonal IgG bands in the CSF as a diagnostic marker[12,13].

Previous studies investigated the effect of B cell depletion on specific immune subsets using hypothesis driven flow cytometry-based methods[14,15]. In this study, we sought to explore the diverse immune landscape and cell states with "*in vivo* perturbation" in patients with MS by measuring immune phenotypes with scRNAseq transcriptomic granularity. B cell depletion in patients was accomplished with systematic removal of naïve and memory B cells through a humanized anti-CD20 antibody, ocrelizumab. We performed 5' scRNAseq on 18 paired peripheral blood mononuclear cells (PBMC) and paired CSF samples obtained from incident MS patients pre- and post- B cell depletion treatment followed by flow cytometry validation of protein expression. The high dimensional single-cell data set allowed for simultaneous interrogation of the diverse immune populations in patient blood and CSF across tissue types, disease states and treatment status.

Our data revealed increased frequency of a CSF macrophage population that exhibited anti-inflammatory transcriptomic signatures post-B cell depletion therapy. In the periphery, we discovered that $CD16^+$ monocytes showed the highest upregulation of transcriptomic TNFα/NFκB signatures after ocrelizumab treatment compared to other cell types. The transcriptional changes were confirmed with increases in TNFα protein in monocytes consistent with the finding that anti-TNFα treatment increases MS disease activity. Moreover, changes in the myeloid compartment were accompanied by increases in TIGIT expressing $FoxP3^+$ Tregs and decreases in the frequency of circulating, myelin reactive $CD4^+$ T cells. Thus, we defined the immune cell states associated with remission and demonstrate that B cell depletion achieves therapeutic efficacy in early MS through modulating in parallel the innate and adaptive immune compartments.

Results

$CD14^+CD68^+$ CSF cells increase in frequency post B cell depletion therapy

All patients were treatment naïve to any immunomodulatory therapy with new onset relapsing remitting MS (Supplementary Table 1). To elucidate the effects of anti-CD20 treatment on the CNS microenvironment, we interrogated five CSF samples from people with relapsing remitting MS (RRMS) pre- and post- B cell depletion treatment and performed an additional comparison with six CSF samples from age-matched healthy donors. All pre-treatment samples were collected from treatment-naïve patients, while post-treatment CSF samples were obtained at different time points: two at 6-month post-treatment, two at 12-month post-treatment, and one at 18-month post-treatment (Supplementary Table 1). After QC of low-quality cells, scRNAseq yielded 60,704 total single cells from 16 CSF samples, including 15,122 cells from six healthy donor samples, 28,493 cells from five MS treatment-naïve samples and 17,089 cells from five MS post- treatment samples (Fig 1a).

After normalization and Harmony batch correction (see Methods), CSF cells were classified into 17 clusters (Fig 1b). To assess potential donor and sample variability, the frequencies of all immune populations in the CSF within each patient were profiled. Across all five patients, pre-treatment MS samples had consistently lower cell frequencies in the $CD14^+CD68^+$ myeloid-1 (Mac 1) cluster compared to healthy donors, and the frequencies of this cluster subsequently increased in all patients after B cell depletion treatment (Fig 1c and Supplementary Fig1). In parallel, from all five patients, 1536 B cells were found pre-treatment and only 188 B cells were detected post treatment, as expected due to the mode of action of anti-CD20 therapies. To further identify the immune subset most affected by B cell depletion therapy, we used MELD[16] to quantify the effect of B cell depletion treatment on all immune cell clusters in the CSF and discovered that the same Mac 1 cluster was the most enriched cell type after treatment (Fig 1d). While the dendritic cell clusters exhibited similar trends of increased frequency post-treatment as the Mac 1 cluster, we prioritized downstream analyses on the Mac 1 subset as it had the highest MELD enrichment score and the least MELD score variability across patients.

$CD14^+CD68^+$ CSF cells are CSF- specific macrophages with microglia gene signatures

Previous studies reported $CD14^+$ CSF cells in various disease settings[17-19]. We aimed to further evaluate the myeloid transcriptomic signatures in our patient CSF samples to define the

108 CD14$^+$CD68$^+$ myeloid clusters. Mac 1 cluster exhibited high levels of microglia (*TREM2, SPI1,*
109 *CD68, MEF2C*) and monocyte (*CD14, FCGR3A, CSF1R, HLA-DRA*) transcriptomic signatures,
110 while lacking hallmark microglial genes such as *SALL1*, *P2RY12, FCRLS* and *TMEM119*. In
111 addition to pan-macrophage lineage markers *HLA-DR* and *CD14*, Mac 1 cluster also exhibited
112 high expression of *APOE, CSF1R*, and genes that are expressed in extra parenchymal CSF
113 macrophages such as *CST, TGFB1, MS4A7, LYZ, CLEC7A*. The mixture of microglial-like and
114 monocytic genes and the abundant expression of *C1Q* and *HLA* class II genes classified this
115 cluster as CSF-specific macrophages, distinct from monocytes, microglia and macrophages in
116 other CNS tissues (Fig 1e)[20]. Interestingly, memory CD4 cluster 5 exhibited a similar (albeit
117 muted) signature, leading to the initial co-clustering of those two clusters despite coming from two
118 separate lineages (Supplementary Fig 2a, b and Methods).

119 To further delineate the CSF macrophage subset, we computed pan-macrophage (*CD44,*
120 *CCR2, CD45, CD206, CD163, CD274, CD169, MYB*), CNS macrophage (*TGFBI, MS4A7,*
121 *MS4A6C, LYZ2, CD163, P2RX7, CST, CLEC7A*), and microglia (*P2Y12R, TMEM119, TREM2,*
122 *CD115, CD172A, CD91, SPI1, FCRLS, SALL1, HEXB, SIGLECH, SLC2A5*) subset-specific gene
123 modules to evaluate module scores on all myeloid clusters in the CSF. The post-treatment
124 enriched Mac 1 cluster scored the highest on the microglia module compared to other myeloid
125 clusters. In contrast, CD14$^+$CD68$^+$ myeloid-2 (Mac 2) cluster scored higher on the pan-
126 macrophage module compared to others (Fig 1f). Collectively, these transcriptomic signatures
127 reflect the phenotypic diversity of the macrophage compartment in the CSF, and that anti-CD20
128 treatment increased the frequency of a specific subset of microglia-like macrophages within the
129 CSF.

130 **B cell depletion induces an anti-inflammatory phenotype in CSF macrophages**

131 With the recent identification of CSF-specific macrophages[20] and the limited availability of
132 patient CSF samples, the role of CSF macrophages in homeostasis and during MS pathogenesis
133 remains unclear. To better understand the treatment effect of B cell depletion on CSF
134 macrophage immunophenotype, we performed differential gene expression (DE) analysis of pre-
135 and post- treatment MS samples along with healthy donor CSF (Fig 2a). In the enriched Mac 1
136 cluster, hierarchical clustering on differentially expressed genes in MS pre-treatment vs healthy
137 donor cells revealed extensive changes, segregating cells from the two groups and highlighting
138 alterations in MS patients (Supplementary Fig 3a). In contrast, only 82 genes were differentially

139 expressed between MS pre- and post- treatment CSF macrophages, therefore grouping CSF
140 macrophages from patients together by hierarchical clustering despite treatment status
141 (Supplementary Fig 3b). Among the 60 genes upregulated after B cell depletion are *EGR1* that
142 represses macrophage activation[21], *ZFP36* and *ZFP36L1* that modulate post-transcriptional
143 regulation of immune responses and oxidative phosphorylation genes (*NDUFA13, UQCRB,*
144 *NDUFB1, ATP5F1E*) that are associated with anti-inflammatory macrophages[22,23]. In addition,
145 genes involved in migration and endocytosis (*SLC11A1, ITGB2, CSF1R, DAB2, NUMB, RAB11A,*
146 *ANXA1, APOE*) were downregulated after B cell depletion (Fig 2a).

147 We observed increases in HLA class I and class II mRNA expression in Mac 1 cells from
148 baseline MS patient CSF as compared to healthy CSF Mac 1 cells. These increases in MHC
149 expression from patients with MS decreased after B cell depletion (Fig 2b). In contrast, CD83, a
150 macrophage immune checkpoint marker that contributes to the resolution of inflammation and
151 can induce Tregs in experimental models of MS[24-26], was downregulated in MS pre-treatment
152 cells, and recovered to healthy donor levels post- B cell depletion treatment (Fig 2c). We next
153 applied the classical and alternative macrophage activation paradigm to delineate the
154 neuroinflammatory state of CSF macrophages. Post- treatment Mac 1 cells exhibited
155 transcriptomic downregulation in pro-inflammatory programming (*CCR7, JAK1, STAT1, IL1B,*
156 *TNF, TLR4, CD86*) and upregulation of anti-inflammatory genes (*IL-10, TGFB, CLEC7A*) In
157 addition, we observed decrease of macrophage scavenger receptors (*CD163, MRC1, MSR1*) (Fig
158 2d). Taken together, the decreases in MHC class I and class II gene module scores suggest that
159 B cell depletion reduces the probability of T cell activation through CSF macrophage antigen
160 presentation. The increased expression in *CD83, TGFB, IL10*, and the oxidative phosphorylation
161 pathway in CSF macrophages post-treatment suggests that B cell depletion therapy promotes the
162 resolution of inflammatory phenotype in CSF macrophages to restore homeostasis. Lastly, we
163 computed transcriptomic signature scores based on peripheral monocytic gene modules and
164 applied them to the CSF myeloid populations. We found that the enriched Mac 1 cluster scored
165 the highest on the intermediate (*HLADR, CD14, CD11C, CD68, FCGR3A, CX3CR1, CSF1R,*
166 *TLR4*) and nonclassical monocyte (*FCGR3A, CX3CR1, SLAN, CSF1R, CXCR1, CXCR4*) gene
167 modules, whereas Mac 2 scored higher on the classical monocyte (*CD14, CCR2, CCR5, SELL,*
168 *CD36, CD33, CD64*) gene module (Fig 2e). Thus, the transcriptomic resemblance of CSF
169 macrophages to intermediate monocytes prompted us to investigate whether B cell depletion
170 therapy modulates intermediate monocyte frequency in the periphery.

171 **Increased abundance of CD16$^+$ monocytes post B cell depletion in MS patient PBMC**

172 We next investigated whether alterations observed in the CSF post-B cell depletion are
173 recapitulated in peripheral blood. We performed immune profiling with cryopreserved PBMC using
174 scRNAseq from 18 newly diagnosed treatment-naïve patients with relapsing remitting RRMS
175 whose samples were collected for both pre- and 6 months post-treatment (Supplementary Table
176 1, Fig 3a). In our unsupervised analysis we retained 38 communities, which we assigned to
177 coarse-grained immune cell types of interest (naïve T cells, memory CD4$^+$ T cells, cytotoxic
178 lymphocytes, B cells, myeloid cells), and 18 fine-grained cell-types, as described in
179 Supplementary Fig 4a, b and Fig 1b. We classified communities into main lineages based on
180 marker gene inspection and scoring cells against reference datasets using singleR software
181 (Supplementary Fig 4c)[27].

182 Using MELD, we observed computed differences in abundance between the pre- and post-
183 treatment samples. As expected, ocrelizumab treatment significantly decreased the number of B
184 cells except for plasmablasts, which are known to downregulate CD20 that leads to loss of
185 sensitivity to ocrelizumab-mediated depletion (Fig 3b). Given our CSF data, we next focused our
186 attention on myeloid cells. We observed cellular enrichment in two myeloid clusters: CD16$^+$
187 monocytes and plasmacytoid dendritic cells (pDCs) (Fig 3c). We confirmed these changes by
188 formally testing for variations in frequency across all donors and observed that the increased
189 frequency of CD16$^+$ monocytes was conserved across donors (Fig 3d and Supplementary Fig
190 5a). The CD16$^+$ monocytes cluster was the only cluster with detectable levels of *FCGR3A*, the
191 gene encoding CD16 (Supplementary Fig 5b and d), and displayed markers associated with
192 intermediate and non-classical monocytes. Scoring against the Monaco Immune reference with
193 singleR revealed strong enrichment in intermediate and non-classical reference transcriptomes
194 (Supplementary Fig 5c). To confirm this change in abundance we measured circulating
195 frequencies of various monocyte subpopulations using flow cytometry (Supplementary Fig 6a).
196 While there was no significant difference after B cell depletion in CD14$^+$CD16$^-$ monocytes, there
197 was a significant increase in CD14$^+$CD16$^+$ monocytes with treatment (Fig 3e).

198 **Increased activation and TNFα production in CD16$^+$ monocytes post B cell depletion**

199 We next determined whether CD16$^+$ monocytes harbor an altered transcriptomic state
200 after B cell depletion. We computed differentially expressed genes while controlling for inter-
201 individual variation using a generalized linear mixed model (glmm, as implemented in NEBULA[28].

202 We observed an increased expression of soluble molecules (*CCL5, CXCL8, TNFA*), surface
203 receptors (*CD83, ITGB2, ITGA2B*), and NFκB signaling pathway (*TRAF1, NFKB2, REL, RELB,*
204 *NFKBIA*) (Fig 4a). CD16$^+$ monocytes showed downregulation in major transcription factors
205 (*RXRA, IKZF1, KLF4, IRF4*) and CD81, a marker that facilitates monocytes homing to the CNS
206 in EAE[29]. Given the activated transcriptomic signature observed in CD16$^+$ monocytes, we
207 validated changes at the protein level and observed downregulation of CD81, and upregulation
208 of monocyte activation marker HLA-DR using flow cytometry (Fig 4b).

209 Given the presence of differentially expressed genes from the NFκB signaling pathway, we
210 next performed GSEA analysis in the enriched CD16$^+$ monocyte cluster using the Hallmark gene
211 sets collection. Consistent with these findings, we observed enrichment in TNF-NFκB pathway
212 (Fig 4c), as well as downregulation related to JAK-STAT signaling gene sets (IL-2, STAT5, IL-6,
213 JAK, STAT3, interferon alpha and interferon gamma signaling) post-treatment. Finally, to
214 determine whether these pathway modulations can also be observed in CSF macrophages
215 (described in Figure 2), we created custom gene sets based on PBMC DE and ran GSEA on the
216 enriched Mac 1 CSF macrophages to test for gene signature enrichment. We observed a positive
217 enrichment of blood-upregulated genes in the CSF, while blood-downregulated genes showed no
218 significant enrichment in the CNS (Fig 4d). These data suggest that while B cell depletion therapy
219 upregulates similar biological signatures in the CNS and periphery, the treatment-mediated *in vivo*
220 perturbation of biological pathways is tissue-dependent and informed by the local environment.

221 **B cell depletion induces ubiquitous response to TNFα in PBMC**

222 We next assessed whether the observed upregulation of TNF-NFκB pathway post-
223 treatment is cell-type specific. We computed differentially expressed genes for pre- vs post- B cell
224 depletion in all clusters and used DE results to run GSEA analysis. We observed TNF-NFκB
225 pathway activation across most immune cell types post-ocrelizumab treatment (Fig 5a). However,
226 the downregulation of JAK-STAT related pathways was restricted to CD16$^+$ monocytes, and the
227 remaining or repopulating B cells post-treatment showed increased expression of various gene
228 sets related to cell survival (P53 pathway, apoptosis), metabolism (cholesterol homeostasis) and
229 JAK-STAT signaling (IL2 STAT5 signaling, IL6 JAK STAT3 signaling). Interestingly, clustering
230 communities based on GSEA leading edge genes similarity showed that the NFκB signaling
231 enrichment was most similar between B cells and myeloid cells while T lymphocytes formed a

232 separate cluster, suggesting that transcriptomic responses to NFκB signaling differ between those
233 lineages (Fig 5b).

234 Despite the ubiquitous TNF-NFκB pathway activation across cell types, $CD16^+$ monocytes
235 showed the highest pre-treatment transcriptomic expression of TNFα and sustained the
236 upregulated expression after treatment (Fig 5c). We also detected an increased expression of
237 TNFα in B cells cluster 3, MAIT, and DC clusters. To confirm changes in TNFα expression at the
238 protein level, we enriched $CD14^+$ or $CD16^+$ monocytes from cryopreserved PBMCs and showed
239 that LPS-stimulated monocytes from MS patients expressed more TNFα post B cell depletion (Fig
240 5d). Increases of TNFα production by LPS-stimulated $CD14^+$ cells was similarly observed in MS
241 patients treated with ocrelizumab by another group[30]. However, there was no significant difference
242 in TNFα ELISA using culture supernatant (data not shown).

243 **B cell depletion therapy reprograms the $CD4^+$ T helper cell compartment in both CSF and**
244 **PBMC**

245 Though $CD4^+$ T cells are thought to play a central role in MS pathophysiology, limited
246 changes were observed in the $CD4^+$ T cell compartment using singleR, MonacoImmune, and
247 manual cellular annotation methods. Therefore, we applied a recently developed framework that
248 captures a more granular classification and qualitative assessment of $CD4^+$ T cells based on
249 scRNAseq data (Fig 6a)[31]. This novel framework assigned CD4 T cells into five major clusters
250 (cluster Layer 1 or L1) and 18 minor clusters (cluster L2) by Symphony reference mapping (Fig
251 6b, Supplementary Fig 7a and 8a), and measured the activities of 12 pre-defined transcriptomic
252 gene programs of $CD4^+$ T cells using non-negative matrix factorization projection (NMFproj).

253 At the major cluster L1 level, we did not detect any significant cell frequency changes in both
254 CSF and PBMC (Supplementary Fig 7b and 8b). However, at the minor cluster L2 level, there
255 was a significant reduction of $CD4^+$ T effector memory (Tem) expressing T peripheral helper (Tph)
256 markers (Tem -Tph; *PDCD1*^{lo}*CXCR5*$^+$) in both CSF (padj= 1.88×10^{-2}) and PBMC (padj= $9.41 \times 10^{-}$
257 ^{6}) tissues after B cell depletion treatment (Fig 6c and d, Supplementary Fig 7c and 8c). In CSF
258 alone, the frequency of $CD4^+$ T central memory (Tcm) expressing T follicular helper (Tfh) markers
259 (Tcm -Tfh; *PDCD1*$^+$*CXCR5*$^+$) was significantly reduced (padj=9.36×10^{-3}) while the frequency of
260 Tcm-Th0 was increased (padj=0.0472), suggesting a shift toward a naïve phenotype post- B cell
261 depletion in the CNS (Fig 6c and d, Supplementary Fig 7c and 8c). We also observed a significant
262 increase of $CD4^+$ naive T cells expressing *SOX4* (Tnaive *SOX4*; *SOX4*$^+$*PECAM1*$^+$) (padj=$4.29 \times 10^{-}$
263 ^{3}) in the blood, which is a recent thymic emigrant population[32], indicating that the peripheral blood

264 $CD4^+$ T cell pool has been replenished by newly generated $CD4^+$ T cells after the treatment (Fig
265 6d, Supplementary Fig 8c).

266 We then assessed the changes in gene program activity quantified by NMFproj in each L2
267 subpopulation. We observed a significant reduction in cell types for NMF6 (Tfh-Feature or Tfh-F;
268 *MAF*, *CXCR5*) and NMF11 (Th1-F; *GZMK*, *EOMES*) post-treatment in both blood and CSF. (Fig
269 6e and f, Supplementary Data 1 and 2). Because NMF6 (Tfh-F) is predominantly high in Tcm-Tfh,
270 Tem-Tph, and intermediate Treg (Treg Int), the decrease of NMF6 (Tfh-F) in both tissues indicates
271 that B cell depletion treatment reduces their frequencies and potentially represses the
272 repopulation of these CD4 subtypes quantitatively and qualitatively. An increase of NMF2 (Th17-
273 F; *RORC*, *CCR6*) in the Tem population was observed in CSF, whereas NMF2 signature
274 decreased in the blood (Fig 6e and f, Supplementary Data 1 and 2). We also observed increased
275 NMF10 (Tissue-F; *JUNB*, *NFKBIA*) in blood after treatment (Fig. 6f, Supplementary Data 2).
276 These observations suggested a redistribution of the $CD4^+$ T subsets between the periphery and
277 CNS. Altogether, these findings demonstrate that B cell depletion notably alters the $CD4^+$ T cell
278 compartment by reducing specific T cell populations such as Treg Int, Tcm-Tfh, and Tem-Tph and
279 modifying effector gene expression profiles such as repression of NMF6 (Tfh-F) and NMF11 (Th1-
280 F), which may be associated with its therapeutic efficacy in MS.

281 **B cell depletion increases suppressive Tregs**

282 Loss of Treg function has been repeatedly observed in patients with MS[8,33], and we showed
283 MS susceptibility variant modulate can modulate Treg function[34]. We sub-clustered Tregs from
284 scRNAseq PBMC data and compared L2 subpopulation frequencies to examine Treg alterations
285 in more detail. We observed a significant decrease in naïve Tregs (Treg Naive) (*FOXP3, CCR7*,
286 padj= 3.13×10^{-2}) and Treg Int (*FOXP3*, *FCRL3*, padj=6.79×10^{-3}) and an increase in effector Treg
287 (Treg Eff) (*HLA-DR*s, *CD74*, padj=2.33×10^{-3}) in post-treatment samples. (Fig 7a and b). We also
288 examined gene expression differences in the whole Treg population and found that *HLA-DR*s and
289 *CD74*, which are the markers of Treg Eff, were increased. In contrast, *FCRL3*, a marker of Treg
290 Int, was decreased after treatment (Fig 7c, Supplementary Fig 9a and b). These data suggest
291 that B cell depletion skewed the Treg function toward the effector phenotype. Next, we examined
292 the potential mediators of myeloid-Treg interactions using ligand-receptor prediction analysis (Fig
293 7d). Since TNF is known to enhance the function of Tregs through interaction with TNFR2, which
294 is abundant in Tregs[35,36], we hypothesized that monocytes upregulated *TNF* expression following
295 B cell depletion and promoted Treg expansion through TNFR2 signaling. We measured Treg

296 frequency using flow cytometry in MS patient PBMC pre- and post- ocrelizumab treatment. We
297 observed a significant increase in the frequency ($p < 0.0001$) of Tregs (Fig 7e) in post-treatment
298 PBMC samples. TIGIT protein is highly expressed in Treg Eff[37] (Supplementary Fig 9b and c) and
299 has been shown to associate with increases in functional activity in human and mice[38,39].
300 Therefore, we measured the frequency of TIGIT expressing Tregs after B cell depletion and
301 observed a significant increase post- ocrelizumab treatment (Fig 7f). In summary, these data
302 indicate that B cell depletion corrects for the loss of immune regulation in MS by increasing Treg
303 frequency and effector function.

304 **B cell depletion decreases myelin tetramer binding $CD4^+$ T cells**

305 We and others have shown increases in the frequency of inflammatory myelin reactive T
306 cells recognizing a number of myelin antigens, presumably as a consequence of epitope
307 spreading, in the circulation of MS patients. We have demonstrated the utility of using a panel of
308 MHC class II tetramers loaded with myelin epitopes from myelin basic protein (MBP), proteolipid
309 protein (PLP), and myelin oligodendrocyte glycoprotein (MOG) to directly measure the frequency
310 of autoreactive T cells in the disease[4,5,40,41]. To increase the accuracy of detecting autoreactive T
311 cells, we used both PE- and APC-conjugated tetramers with the same myelin composition
312 (Supplementary Fig 6b). We initially examined a cohort of patients pre- and post-B cell depletion
313 and observed a marked decrease in the frequency of myelin PE- and APC-tetramer double
314 positive (Tetramer DP) $CD4^+$ T cells (Fig 7g). In these data, decreased frequencies of CD45RA-
315 $CXCR5^+$ cells and $CCR6^+CXCR3^-$ cells were observed in myelin tetramer binding $CD4^+$ T cells
316 (Fig 7h). Longitudinal kinetic analysis using fresh PBMC derived from a separate MS cohort
317 (Supplementary Table 1) revealed significant decreases in the frequency of these autoreactive
318 $CCR6^+CXCR3^+$ $CD4^+$ T cells at 6 months post-treatment with no significant changes in
319 $CCR6^+CXCR3^+$ cells in non-tetramer reactive $CD4^+$ T cells. This trend continued through 52
320 weeks (Fig 7i). These results indicate that B cell depletion directly or indirectly regulates the
321 frequency of presumably pathogenic myelin reactive T cells.

322

323 **Discussion**

324 We performed an unbiased analysis of the immune landscape using scRNAseq after *in*
325 *vivo* perturbation of the immune system with B cell depletion therapy in treatment-naïve MS
326 patients. Ocrelizumab, a humanized anti-CD20 monoclonal antibody, induces a systematic
327 removal of naïve and memory B cells with ~98% efficacy in preventing new CNS lesions[3]. Here,
328 we demonstrate that B cell depletion induces cell type-specific recovery of CSF macrophages
329 and intermediate monocytes and reprograms them toward transcriptional phenotypes that
330 resemble healthy donor macrophage and monocytes. Specifically, we identified a novel anti-
331 inflammatory transcriptomic signature in post-treatment MS CSF macrophages, promoting the
332 resolution of inflammation and maintain homeostasis with upregulation of CD83, TGFβ, and IL-
333 10. $CD16^+$ monocytes showed the highest level of TNFα messenger RNA expression pre-
334 treatment, and B cell depletion further increased TNFα protein expression in these monocytes.
335 Furthermore, after B cell depletion, we observed shifts in T cell populations, including decreased
336 frequencies of Tem-Tph and Treg Int, along with Th1- and Tfh-type gene programs. Notably, we
337 found that B cell depletion increased $TIGIT^+$ regulatory T cell frequency and decreased myelin
338 tetramer-binding $CD4^+$ T cell frequency in the blood compartment. Our study provides an
339 extensive transcriptomic map of immunological changes through the simultaneous interrogation
340 of the diverse immune populations perturbed by *in vivo* B cell depletion. This approach enables
341 us to discover distinct cell-type specific mechanisms of action consistent with the remarkable
342 efficacy of B cell depletion therapy in MS.

343 The changes in monocyte frequency after B cell depletion were unexpected and revealed
344 the power of an unbiased systems approach in dissecting the multitudes of immune-regulatory
345 mechanisms of a highly efficacious therapy. We hypothesize that the dichotomous roles of
346 monocytes in the pathogenesis of MS are due to the nature in which myeloid phenotype and
347 function are orchestrated by the metabolic requirements in surrounding tissue environments.
348 Soluble factors and cytokines shape macrophage differentiation and activate molecular programs
349 that either exacerbate or attenuate disease[42]. Systemic depletion of pathogenic B cells likely
350 reduces the inflammatory states of multiple immune cell types in a feedback loop manner, and
351 the subsequent recalibration of the cytokine milieu allows macrophages to differentiate in a
352 steady-state environment and engage in disease-resolving transcription program to restore
353 homeostasis. Given our study is limited to one post-treatment timepoint, it is possible that the
354 changes we describe will normalize on the long term. Our ability to detect functional changes in

355 the CSF compartment were limited by the small sample size, variable post-treatment time-points,
356 and a small number of cells composing the CSF macrophages clusters compared to other
357 immune populations. However, a previous study by Mrdjen et al. dissected changes in myeloid
358 populations in the EAE model and observed CNS-specific alterations of macrophages and
359 microglia phenotypes during the disease course[43]. Interestingly, they noted that border-
360 associated macrophages (BAMs) share similar profiles with pDCs compared to other myeloid
361 subsets. We similarly observed that increased abundance of CSF macrophages was
362 accompanied by increased abundance of pDCs (Fig 1).

363 While the ontogeny of CSF macrophages has not been well elucidated, we posit that some
364 of the enriched macrophage population could derive from blood monocytes as we observed some
365 similarity in transcriptomic kinetics between enriched CSF macrophages and enriched CD16+
366 monocytes post- B cell depletion. With autoimmune exacerbations in patients with MS, peripheral
367 blood monocytes receive inflammatory cytokine signals and cross the blood- brain barrier with T
368 cells leading to CNS lesions[44,45]. While macrophages are the dominant cell type in these lesions,
369 blood monocytes also extravasate into the CSF and differentiate into CSF macrophages[46].
370 However, it is critical to not hyperactivate CSF macrophages in the process of phagocytosing
371 waste to prevent downstream immune activation of autoreactive lymphocytes[47]. With B cell
372 depletion, the decrease in myeloid inflammatory cytokines enables CSF macrophages to receive
373 pro-resolving signals to execute their homeostatic function in mediating tissue repair[48]. Our data
374 suggest an anti-inflammatory phenotype in CSF macrophage after B cell depletion treatment and
375 demonstrate that anti-CD20 depletion therapy restores macrophage gene signatures similar to
376 those of healthy controls. Importantly, the inclusion of healthy donor CSF samples allows us to
377 conclude that anti-CD20 treatment reprograms CSF macrophages toward a homeostatic/healthy
378 cell state.

379 In the peripheral immune compartment, we uncovered a ubiquitous TNFα/NFκB activation
380 signature across a wide range of circulating immune cells post- B cell depletion. $CD14^{+}CD16^{+}$
381 monocytes have been shown to be a potent producer of TNFα[49], and our study suggests that TNF
382 is a pleiotropic cytokine that potentially exerts anti-inflammatory effects after B cell depletion. It
383 has not escaped our attention that B cell depletion confers moderate clinical effectiveness in
384 treating rheumatoid arthritis whereas anti-TNFα clearly worsen MS immunopathogenesis[50]. While
385 the increased production of TNFα with a clinically effective treatment appears to be counter-

386 intuitive, the beneficial role of TNFα in MS is substantiated by clinical trials results showing anti-
387 TNFα treatment in patients led to significant worsening of disease activity[51]. Moreover, molecular
388 dissection of MS risk allele rs1800693 located in the gene encoding the TNFR1 revealed the
389 associated variant that codes for a soluble form of TNFR1, which mimics TNF blocking
390 molecules[52,53], again consistent with the observation that TNFα blockade leads to increased
391 disease activity. In the context of chronic inflammation, this scenario where TNFα bears an anti-
392 inflammatory role is reminiscent of the anti-tumor immune response. Specifically, in the tumor
393 microenvironment, constant exposure to TNFα leads to immunosuppressive responses involving
394 Tregs, B regulatory cells and myeloid-derived suppressor cells[54], and blocking TNF leads to
395 improved response to immune checkpoint blockade in an orthotopic melanoma mouse model[55].
396 Additionally, identifying the precise signaling events leading to the observed transcriptomic
397 changes is challenging given that the main TNFα signaling pathway is through NFκB, a highly
398 ubiquitous signaling pathway. Thus, we cannot exclude other receptors signaling through NFκB
399 are participating to the transcriptomic alterations observed post-treatment. Nevertheless, our rich
400 dataset provides a non-biased road map which can now be investigated in animal models to better
401 elucidate the more detailed mechanisms associated with B cell depletion.

402 Several of the established cell annotation methods that we employed were unable to
403 detect changes in the CD4 T cell compartment. The biologically relevant signals could potentially
404 be obfuscated due to the small frequency of myelin-specific T cells. Applying reference mapping
405 with finer granular reference and gene program quantification by NMF, we were able to detect B
406 cell depletion- mediated modulation of various T cell subsets. While we were able to confirm the
407 increase of effector Treg frequency both by transcriptomic and protein expression, it will be of
408 interest to more precisely identify whether there are differences in specific myelin antigens and
409 other antigens, as recent studies indicate EBV infection of B cells is associated with the onset of
410 MS[56].

411 Our T cell data suggests several mechanisms in which B cell depletion can lead to
412 modulation of T cell functionality. One potential model is that TNFα from myeloid cells engages
413 TNFR2 on Tregs leading to suppression of autoreactive T cells after B cell depletion in RRMS
414 patients. Alternatively, as first shown by Lanzavecchia et al.[57], B cells may be the key antigen
415 presenting cell and their depletion may result in loss of autoreactive effector or memory T cells.
416 Similarly, the decrease of MHC expression on myeloid cells may also support this hypothesis.

417 Rather than identifying one mechanism for the high clinical efficacy of B cell depletion in MS, our
418 unbiased "*in vivo* perturbation" investigation uncovered a number of changes in the immune
419 circuitry. This is perhaps not surprising as the genetic architecture of MS and other autoimmune
420 diseases suggests that multiple pathways are involved in disease pathogenesis[58]. In summary,
421 our unbiased systems analysis identified a series of immunoregulatory pathways induced by B
422 cell depletion. We propose that for B cell depletion to be such a globally effective therapy in MS,
423 essentially subverting the autoimmune attack of the CNS, several mechanisms of action must be
424 involved to maintain homeostasis. It is likely that different immunosuppressive pathways become
425 activated among patients, leading to marked decreases of autoreactive myelin reactive T cells in
426 the blood compartment. Our analyses comparing immune cells in CSF and blood also highlights
427 shared vs distinct changes across compartments, suggesting regulation of CNS homing
428 mechanisms is affected by anti-CD20 therapies. Considering the potential of disease-mediating
429 and homeostatic functions in the myeloid compartment, future analyses can be designed with a
430 myeloid focus using fresh tissue for higher sensitivity in protein detection. Nevertheless, these
431 datasets and observations provide a critical starting point that will require well-designed *in vitro*
432 and *ex vivo* assays and appropriate animal models to fully elucidate the perturbational effects of
433 B cell depletion on the functionality of the immune system.

434

Methods

Ethic Statement

This study was approved by the Institutional Review Board at Yale University. CSF and blood samples were obtained from healthy donors and MS patients with informed consent.

Patient Cohorts

All patients had early onset relapsing remitting MS and had not been on previous immunomodulatory treatments. A small subset of patients had received IV solumedrol within 3 months of blood draw. Eighteen patients undergoing single cell RNA seq studies had CSF analysis prior to the initiation of treatment, and five of those subjects had repeat lumbar punctures, as outlined in the results section. A total of six age-matched healthy controls had lumbar punctures, and those results were previously reported[44]. An additional four subjects had flow cytometric analysis only. Patient characteristics are summarized in Supplementary Table 1.

Sample preparation for scRNAseq

Fresh patient CSF samples were centrifuged, and cells were immediately processed using 10x Genomics 5Pv1 chemistry. Samples were collected prior to infusion of B cell depletion therapy. In the CSF sample cohort, four of the patients were administered ocrelizumab B cell depletion treatment, and one was treated with rituximab. Patient PBMCs were isolated from whole blood using Lymphoprep (STEMCELL) density gradient centrifugation. All patients were administered ocrelizumab B cell depletion in the PBMC cohort. Cryopreserved patient-matched pre-treatement and 6-month post-treatment PBMCs were thawed and processed within the same experimental batch using 10x Genomics 5Pv1 chemistry. For PBMCs, TCR libraries were generated along with the gene expression libraries.

scRNAseq QC

PBMC and CSF libraries were sequenced at 20,000 read pairs per cell on Illumina NovaSeq instrument. Fastq files were processed using cellranger version 3.1.0 mapping to GRCh38 human reference genome. Alignment and quantitation were performed with the “cellranger count” command for each emulsion (using the 2020-A 10x genomics human reference), to generate unique molecular identifier (UMI) count matrices.

466 For CSF, Data QC was performed in R using the Seurat package. Low quality cells were
467 filtered out based on mitochondria percent, UMI counts and number of features for individual
468 samples. Samples were then merged, log10-transformed, and batch corrected using Harmony.
469 For PBMCs, we first filtered extreme outliers by excluding droplets with less than 1500
470 UMI counts, or less than 850 unique genes detected. As distribution of those parameters varied
471 across emulsions, we median-centered the log10-transformed number of unique genes detected
472 and removed low quality droplets with less than 1,100 unique genes detected or more than 2.5%
473 mapping of UMI counts mapping to mitochondrial genes. We also removed potential doublets by
474 filtering out droplets with more than 2,600 unique genes detected.
475
476 **scRNAseq analysis**
477 *Dimensionality reduction and clustering*
478 For cells passing quality control, we normalized UMI counts by dividing each count by the
479 total number of counts per cell. We then multiplied normalized counts by 10,000 and added a
480 pseudo count of 1 before log-transformation. We computed the stabilized variance of each gene
481 using the variance-stabilizing transformation (VST) and retained genes with stabilized variance >
482 1 for principal component analysis (PCA). Genes mapping to the T cell receptor (TCR), the B cell
483 receptor (BCR) and the Y chromosome were excluded from PCA analysis. We computed the first
484 50 principal components (PCs) using a partial singular value decomposition method, based on
485 the implicitly restarted Lanczos bidiagonalization algorithm (IRLBA), as implemented in the *Seurat*
486 R package[59]. To correct for systematic differences across samples, we applied harmony
487 integration[60] to the first 50 PC loadings and retained 30 harmony-corrected PCs to build nearest
488 neighbor graphs for visualization using Uniform Manifold Approximation and Projection (UMAP)
489 (minimum distance = 0.5, spread = 10), and community detection using Louvain algorithm, as
490 implemented in *Seurat*. We also computed a relative likelihood of cells being observed in specific
491 experimental conditions using Manifold Enhancement of Latent Dimensions (MELD)[16].
492 We embedded cells into 2 UMAP dimensions and applied Louvain algorithm. We
493 annotated cluster cell types based on individual gene expression and the SingleR automatic
494 annotation package using the MonacoImmuneData PBMC reference[61]. We tested for variation in
495 clusters frequency in the CSF and in the blood separately by modelling the per-sample cluster
496 frequencies using a beta distribution in a generalized linear model framework, as implemented in
497 the *betareg* R package[62].

498

499 *Differential gene expression (DE)*

500 For DE testing at the single cell level in CSF, we tested each gene individually using a
501 generalized linear model approach as implemented in the *speedglm* R package, using a poisson
502 distribution and a log link function[34]. We excluded low expression genes based on a UMI count
503 per cell < 0.005, as well as ribosomal, mitochondrial, TCR, BCR. We evaluated differences in
504 counts with treatment predictor, and a [number of UMIs detected] covariate to account for
505 differences in library size. We then computed shrunk log fold changes using adaptative shrinkage
506 methods implemented in the *ashr* R package[63] (using a mixture of normal distributions) and FDR
507 (Benjamini & Hochberg method) across all genes tested. Genes with FDR < 0.05 were considered
508 differentially expressed. For differential expression testing at the single cell level in PBMCs, we
509 used a negative binomial mixed linear model as implemented in the NEBULA package[28]. We then
510 used shrunken log fold changes as a ranking metrics to run geneset enrichment analysis (GSEA).

511

512 *Treg volcano and ligand-receptor analyses*

513 Volcano plot displaying differential expression analysis performed using *nebula* comparing pre-
514 and post-treatment Treg population. Among genes with differential expression (BH < 0.05) and
515 average expression >0.1, those that encode surface proteins (based on Cell Surface Protein Atlas
516 surfaceome protein database) were selectively labeled[64]. NicheNet (*nichenetr)*[65] was used to
517 identify predicted ligand-receptor interactions between myeloid populations and Tregs, will a
518 particular focus on potential ligands that are differentially regulated in myeloid cells with B cell
519 depletion treatment. Tregs were selected as the "receiver cell type", including all expressed genes
520 as potential receptors. Myeloid cells were selected as the "sender cell type", limiting the set of
521 potential ligands to the combined list of genes differentially expressed with B cell depletion
522 treatment in myeloid cell clusters (see *NEBULA* analysis). Predicted ligand-receptor interactions
523 were displayed as a heat map in which ligands (expressed by myeloid cells) were plotted against
524 receptors (expressed by Tregs) and weighted by prior interaction potential.

525

526 *$CD4^+$ T cell automatic labeling and quantification of gene programs*

527 The PBMC and CSF data were processed using the pipeline developed in the previous study[31] to
528 assign $CD4^+$ T cell clusters. This pipeline employs Azimuth[37] for the extraction of $CD4^+$ T cells and
529 uses Symphony[66] for predicting $CD4^+$ T cell clusters. For interpretability, 'Treg Act' has been
530 renamed to 'Treg Int' from the original literature. We tested for variation in cluster frequency by

531 modeling the per-sample cluster frequencies using a beta distribution in a generalized linear
532 model framework, as implemented in the *betareg* R package. For the assessment of TIGIT protein
533 expression, we used CITE-seq data from PBMCs deposited in GSE164378 and performed
534 reference mapping using the pipeline. Additionally, a 12-dimensional qualitative evaluation was
535 conducted on the extracted $CD4^+$ T cells using NMFproj[67]. We applied a generalized linear model
536 to assess feature changes per cluster[31].
537

538 **Flow cytometry analysis**

539 Frozen PBMCs were used for flow cytometry validation, except longitudinal myelin tetramer
540 staining were performed on fresh PBMCs (n=4). Patient peripheral blood mononuclear cells were
541 stained with a ViaKrome 808 Fixable Viability dye following the manufacturer's instructions. Cells
542 were then labeled with surface antibodies for 30 min at 4°C. For intracellular staining, cells were
543 fixed and permeabilized with BD Cytofix/Cytoperm Buffer (BD Biosciences) for 10 min at room
544 temperature, then washed with phosphate-buffered saline. Intracellular proteins were stained in
545 permeabilization buffer (eBioscience) for 30 min at 4 °C. Antibody details are provided in
546 Supplementary Table 2. For TNF staining, monocytes were enriched from cryopreserved PBMCs
547 using EasySep™ Human Monocyte Enrichment Kit without CD16 Depletion Kit (STEMCELL
548 technologies). Enriched monocytes were stimulated with 100ng/ml LPS for 4h at 37 °C before
549 staining. To investigate myelin tetramer reactive T cells, APC- or PE- conjugated tetramers which
550 were composed by DRB1*15:01 (loaded with MBP, MOG and PLP) or DRB1*04:01 (loaded with
551 MOG and PLP) were used[4,41]. Myelin tetramers were incubated with cells for 30 min at 37°C
552 before staining with antibodies. Cells were acquired on a BD Symphony flow cytometer with
553 FACSDiva (BD Pharmingen) and data were analyzed with FlowJo software v.10 (Treestar).
554

555 **Peptide loading**

556 Biotinylated monomers were diluted to a concentration of 0.5 mg/mL with 0.1 M phosphate buffer
557 and incubated with 0.4 mg/ml of at 37°C for 72 h in the presence of 2.5 mg/ml n-Octyl β-D-
558 glucopyranoside (OG) and 1 mM Pefabloc SC (Sigma–Aldrich, St. Louis, MO). Peptide loaded
559 monomers were subsequently conjugated into tetramers using R-PE streptavidin (ThermoFisher
560 Scientific, Waltham, MA) or fluorochromes of interest at a molar ratio of 8:1. Myelin peptide
561 sequences are listed in the Supplementary Table 3.
562
563

Data and code availability statement:

All raw scRNAseq data generated in this study will be deposited on dbGAP upon acceptance. All code used for genomics analysis will be available on github and figshare, along with intermediate analysis files upon acceptance.

Acknowledgement:

The authors thank Rahul Dhodapkar for helpful discussions on computational data analysis. Chuan He for technical support and Kathryn Miller-Jensen for experimental input and discussion. This work was supported by NIH grants (P01 AI073748, U19 AI089992 U24 AI11867, R01 AI22220, UM 1HG009390, P01 AI039671, P50 CA121974, R01 CA227473) and Race to Erase MS to D.A.H. and National MS Society to D.A.H. and M.R.L. and grants from Genentech and F. Hoffmann-La Roche Ltd as part of Integrative Neuroscience Collaborations Network.

Declaration of Interests

D.A.H. has received research funding from Bristol-Myers Squibb, Novartis, Sanofi, and Genentech. He has been a consultant for Bayer Pharmaceuticals, Repertoire Inc, Bristol Myers Squibb, Compass Therapeutics, EMD Serono, Genentech, Juno therapeutics, Novartis Pharmaceuticals, Proclara Biosciences, Sage Therapeutics, and Sanofi Genzyme. E.E.L. has received research support from Biogen, LabCorp, Intus and Genentech. She has been a consultant for Bristol Myers Squibb, EMD Serono, Genentech, Sanofi Genzyme and NGM Bio.

603 **References**

604 1 Lee, D. S. W., Rojas, O. L. & Gommerman, J. L. B cell depletion therapies in autoimmune
605 disease: advances and mechanistic insights. *Nat Rev Drug Discov* **20**, 179-199,
606 doi:10.1038/s41573-020-00092-2 (2021).
607 2 Pescovitz, M. D. *et al.* Rituximab, B-lymphocyte depletion, and preservation of beta-cell
608 function. *N Engl J Med* **361**, 2143-2152, doi:10.1056/NEJMoa0904452 (2009).
609 3 Hauser, S. L. *et al.* Ocrelizumab versus Interferon Beta-1a in Relapsing Multiple Sclerosis.
610 *N Engl J Med* **376**, 221-234, doi:10.1056/NEJMoa1601277 (2017).
611 4 Cao, Y. *et al.* Functional inflammatory profiles distinguish myelin-reactive T cells from
612 patients with multiple sclerosis. *Sci Transl Med* **7**, 287ra274,
613 doi:10.1126/scitranslmed.aaa8038 (2015).
614 5 Ota, K. *et al.* T-cell recognition of an immunodominant myelin basic protein epitope in
615 multiple sclerosis. *Nature* **346**, 183-187, doi:10.1038/346183a0 (1990).
616 6 Dominguez-Villar, M., Baecher-Allan, C. M. & Hafler, D. A. Identification of T helper type
617 1-like, Foxp3+ regulatory T cells in human autoimmune disease. *Nat Med* **17**, 673-675,
618 doi:10.1038/nm.2389 (2011).
619 7 Sumida, T. *et al.* Activated beta-catenin in Foxp3(+) regulatory T cells links inflammatory
620 environments to autoimmunity. *Nat Immunol* **19**, 1391-1402, doi:10.1038/s41590-018-
621 0236-6 (2018).
622 8 Viglietta, V., Baecher-Allan, C., Weiner, H. L. & Hafler, D. A. Loss of functional suppression
623 by CD4+CD25+ regulatory T cells in patients with multiple sclerosis. *J Exp Med* **199**, 971-
624 979, doi:10.1084/jem.20031579 (2004).
625 9 Jain, R. W. & Yong, V. W. B cells in central nervous system disease: diversity, locations and
626 pathophysiology. *Nat Rev Immunol* **22**, 513-524, doi:10.1038/s41577-021-00652-6
627 (2022).
628 10 Lucchinetti, C. F. *et al.* Inflammatory cortical demyelination in early multiple sclerosis. *N*
629 *Engl J Med* **365**, 2188-2197, doi:10.1056/NEJMoa1100648 (2011).
630 11 Magliozzi, R. *et al.* Meningeal B-cell follicles in secondary progressive multiple sclerosis
631 associate with early onset of disease and severe cortical pathology. *Brain* **130**, 1089-1104,
632 doi:10.1093/brain/awm038 (2007).
633 12 Comi, G. *et al.* Role of B Cells in Multiple Sclerosis and Related Disorders. *Ann Neurol* **89**,
634 13-23, doi:10.1002/ana.25927 (2021).
635 13 Reich, D. S., Lucchinetti, C. F. & Calabresi, P. A. Multiple Sclerosis. *N Engl J Med* **378**, 169-
636 180, doi:10.1056/NEJMra1401483 (2018).
637 14 Nissimov, N. *et al.* B cells reappear less mature and more activated after their anti-CD20-
638 mediated depletion in multiple sclerosis. *Proc Natl Acad Sci U S A* **117**, 25690-25699,
639 doi:10.1073/pnas.2012249117 (2020).
640 15 von Essen, M. R. *et al.* Ofatumumab Modulates Inflammatory T Cell Responses and
641 Migratory Potential in Patients With Multiple Sclerosis. *Neurol Neuroimmunol*
642 *Neuroinflamm* **9**, doi:10.1212/NXI.0000000000200004 (2022).
643 16 Burkhardt, D. B. *et al.* Quantifying the effect of experimental perturbations at single-cell
644 resolution. *Nat Biotechnol* **39**, 619-629, doi:10.1038/s41587-020-00803-5 (2021).

645 17 Esaulova, E. *et al.* Single-cell RNA-seq analysis of human CSF microglia and myeloid cells
646 in neuroinflammation. *Neurol Neuroimmunol Neuroinflamm* **7**,
647 doi:10.1212/NXI.0000000000000732 (2020).
648 18 Farhadian, S. F. *et al.* Single-cell RNA sequencing reveals microglia-like cells in
649 cerebrospinal fluid during virologically suppressed HIV. *JCI Insight* **3**,
650 doi:10.1172/jci.insight.121718 (2018).
651 19 Ramesh, A. *et al.* A pathogenic and clonally expanded B cell transcriptome in active
652 multiple sclerosis. *Proc Natl Acad Sci U S A* **117**, 22932-22943,
653 doi:10.1073/pnas.2008523117 (2020).
654 20 Munro, D. A. D., Movahedi, K. & Priller, J. Macrophage compartmentalization in the brain
655 and cerebrospinal fluid system. *Sci Immunol* **7**, eabk0391,
656 doi:10.1126/sciimmunol.abk0391 (2022).
657 21 Trizzino, M. *et al.* EGR1 is a gatekeeper of inflammatory enhancers in human
658 macrophages. *Sci Adv* **7**, doi:10.1126/sciadv.aaz8836 (2021).
659 22 Ip, W. K. E., Hoshi, N., Shouval, D. S., Snapper, S. & Medzhitov, R. Anti-inflammatory effect
660 of IL-10 mediated by metabolic reprogramming of macrophages. *Science* **356**, 513-519,
661 doi:10.1126/science.aal3535 (2017).
662 23 Wculek, S. K. *et al.* Oxidative phosphorylation selectively orchestrates tissue macrophage
663 homeostasis. *Immunity* **56**, 516-530 e519, doi:10.1016/j.immuni.2023.01.011 (2023).
664 24 Grosche, L. *et al.* The CD83 Molecule - An Important Immune Checkpoint. *Front Immunol*
665 **11**, 721, doi:10.3389/fimmu.2020.00721 (2020).
666 25 Burke, J. R. *et al.* Autoimmune pathways in mice and humans are blocked by
667 pharmacological stabilization of the TYK2 pseudokinase domain. *Sci. Transl. Med.* **11**,
668 doi:10.1126/scitranslmed.aaw1736 (2019).
669 26 Peckert-Maier, K. *et al.* CD83 expressed by macrophages is an important immune
670 checkpoint molecule for the resolution of inflammation. *Front Immunol* **14**, 1085742,
671 doi:10.3389/fimmu.2023.1085742 (2023).
672 27 Aran, D. *et al.* Reference-based analysis of lung single-cell sequencing reveals a
673 transitional profibrotic macrophage. *Nat Immunol* **20**, 163-172, doi:10.1038/s41590-018-
674 0276-y (2019).
675 28 He, L. *et al.* NEBULA is a fast negative binomial mixed model for differential or co-
676 expression analysis of large-scale multi-subject single-cell data. *Commun Biol* **4**, 629,
677 doi:10.1038/s42003-021-02146-6 (2021).
678 29 Dijkstra, S. *et al.* Targeting the tetraspanin CD81 blocks monocyte transmigration and
679 ameliorates EAE. *Neurobiol Dis* **31**, 413-421, doi:10.1016/j.nbd.2008.05.018 (2008).
680 30 Geladaris, A. *et al.* IL-10-providing B cells govern pro-inflammatory activity of
681 macrophages and microglia in CNS autoimmunity. *Acta Neuropathol* **145**, 461-477,
682 doi:10.1007/s00401-023-02552-6 (2023).
683 31 Yasumizu, Y. *et al.* Single-cell transcriptome landscape of circulating CD4(+) T cell
684 populations in autoimmune diseases. *Cell Genom* **4**, 100473,
685 doi:10.1016/j.xgen.2023.100473 (2024).
686 32 Kimmig, S. *et al.* Two subsets of naive T helper cells with distinct T cell receptor excision
687 circle content in human adult peripheral blood. *J Exp Med* **195**, 789-794,
688 doi:10.1084/jem.20011756 (2002).

689 33 Dominguez-Villar, M. & Hafler, D. A. Regulatory T cells in autoimmune disease. *Nat*
690 *Immunol* **19**, 665-673, doi:10.1038/s41590-018-0120-4 (2018).
691 34 Axisa, P. P. *et al.* A multiple sclerosis-protective coding variant reveals an essential role
692 for HDAC7 in regulatory T cells. *Sci Transl Med* **14**, eabl3651,
693 doi:10.1126/scitranslmed.abl3651 (2022).
694 35 Chen, X. *et al.* TNFR2 is critical for the stabilization of the CD4+Foxp3+ regulatory T. cell
695 phenotype in the inflammatory environment. *J Immunol* **190**, 1076-1084,
696 doi:10.4049/jimmunol.1202659 (2013).
697 36 Torrey, H. *et al.* A novel TNFR2 agonist antibody expands highly potent regulatory T cells.
698 *Sci Signal* **13**, doi:10.1126/scisignal.aba9600 (2020).
699 37 Hao, Y. *et al.* Integrated analysis of multimodal single-cell data. *Cell* **184**, 3573-3587
700 e3529, doi:10.1016/j.cell.2021.04.048 (2021).
701 38 Joller, N. *et al.* Treg cells expressing the coinhibitory molecule TIGIT selectively inhibit
702 proinflammatory Th1 and Th17 cell responses. *Immunity* **40**, 569-581,
703 doi:10.1016/j.immuni.2014.02.012 (2014).
704 39 Lucca, L. E. *et al.* TIGIT signaling restores suppressor function of Th1 Tregs. *JCI Insight* **4**,
705 doi:10.1172/jci.insight.124427 (2019).
706 40 Markovic-Plese, S. *et al.* T cell recognition of immunodominant and cryptic proteolipid
707 protein epitopes in humans. *J Immunol* **155**, 982-992 (1995).
708 41 Raddassi, K. *et al.* Increased frequencies of myelin oligodendrocyte glycoprotein/MHC
709 class II-binding CD4 cells in patients with multiple sclerosis. *J Immunol* **187**, 1039-1046,
710 doi:10.4049/jimmunol.1001543 (2011).
711 42 Park, M. D., Silvin, A., Ginhoux, F. & Merad, M. Macrophages in health and disease. *Cell*
712 **185**, 4259-4279, doi:10.1016/j.cell.2022.10.007 (2022).
713 43 Mrdjen, D. *et al.* High-Dimensional Single-Cell Mapping of Central Nervous System
714 Immune Cells Reveals Distinct Myeloid Subsets in Health, Aging, and Disease. *Immunity*
715 **48**, 380-395 e386, doi:10.1016/j.immuni.2018.01.011 (2018).
716 44 Pappalardo, J. L. *et al.* Transcriptomic and clonal characterization of T cells in the human
717 central nervous system. *Sci Immunol* **5**, doi:10.1126/sciimmunol.abb8786 (2020).
718 45 Goverman, J. Autoimmune T cell responses in the central nervous system. *Nat Rev*
719 *Immunol* **9**, 393-407, doi:10.1038/nri2550 (2009).
720 46 Herz, J., Filiano, A. J., Wiltbank, A. T., Yogev, N. & Kipnis, J. Myeloid Cells in the Central
721 Nervous System. *Immunity* **46**, 943-956, doi:10.1016/j.immuni.2017.06.007 (2017).
722 47 Monney, L. *et al.* Th1-specific cell surface protein Tim-3 regulates macrophage activation
723 and severity of an autoimmune disease. *Nature* **415**, 536-541, doi:10.1038/415536a
724 (2002).
725 48 Li, R. *et al.* Proinflammatory GM-CSF-producing B cells in multiple sclerosis and B cell
726 depletion therapy. *Sci Transl Med* **7**, 310ra166, doi:10.1126/scitranslmed.aab4176
727 (2015).
728 49 Belge, K. U. *et al.* The proinflammatory CD14+CD16+DR++ monocytes are a major source
729 of TNF. *J Immunol* **168**, 3536-3542, doi:10.4049/jimmunol.168.7.3536 (2002).
730 50 Li, P., Zheng, Y. & Chen, X. Drugs for Autoimmune Inflammatory Diseases: From Small
731 Molecule Compounds to Anti-TNF Biologics. *Front Pharmacol* **8**, 460,
732 doi:10.3389/fphar.2017.00460 (2017).

733 51 Kunchok, A. *et al.* Association Between Tumor Necrosis Factor Inhibitor Exposure and
734 Inflammatory Central Nervous System Events. *JAMA Neurol* **77**, 937-946,
735 doi:10.1001/jamaneurol.2020.1162 (2020).
736 52 Gregory, A. P. *et al.* TNF receptor 1 genetic risk mirrors outcome of anti-TNF therapy in
737 multiple sclerosis. *Nature* **488**, 508-511, doi:10.1038/nature11307 (2012).
738 53 Harroud, A. & Hafler, D. A. Common genetic factors among autoimmune diseases. *Science*
739 **380**, 485-490, doi:10.1126/science.adg2992 (2023).
740 54 Montfort, A. *et al.* The TNF Paradox in Cancer Progression and Immunotherapy. *Front*
741 *Immunol* **10**, 1818, doi:10.3389/fimmu.2019.01818 (2019).
742 55 Bertrand, F. *et al.* TNFalpha blockade overcomes resistance to anti-PD-1 in experimental
743 melanoma. *Nat Commun* **8**, 2256, doi:10.1038/s41467-017-02358-7 (2017).
744 56 Bjornevik, K. *et al.* Longitudinal analysis reveals high prevalence of Epstein-Barr virus
745 associated with multiple sclerosis. *Science* **375**, 296-301, doi:10.1126/science.abj8222
746 (2022).
747 57 Lanzavecchia, A. Antigen-specific interaction between T and B cells. *Nature* **314**, 537-539,
748 doi:10.1038/314537a0 (1985).
749 58 Pisetsky, D. S. Pathogenesis of autoimmune disease. *Nat Rev Nephrol* **19**, 509-524,
750 doi:10.1038/s41581-023-00720-1 (2023).
751 59 Butler, A., Hoffman, P., Smibert, P., Papalexi, E. & Satija, R. Integrating single-cell
752 transcriptomic data across different conditions, technologies, and species. *Nat Biotechnol*
753 **36**, 411-420, doi:10.1038/nbt.4096 (2018).
754 60 Korsunsky, I. *et al.* Fast, sensitive and accurate integration of single-cell data with
755 Harmony. *Nat Methods* **16**, 1289-1296, doi:10.1038/s41592-019-0619-0 (2019).
756 61 Monaco, G. *et al.* RNA-Seq Signatures Normalized by mRNA Abundance Allow Absolute
757 Deconvolution of Human Immune Cell Types. *Cell Rep* **26**, 1627-1640 e1627,
758 doi:10.1016/j.celrep.2019.01.041 (2019).
759 62 Cribari-Neto, F. & Zeileis, A. Beta Regression in R. *J Stat Softw* **34**, 1-24 (2010).
760 63 Stephens, M. False discovery rates: a new deal. *Biostatistics* **18**, 275-294,
761 doi:10.1093/biostatistics/kxw041 (2017).
762 64 Bausch-Fluck, D. *et al.* A mass spectrometric-derived cell surface protein atlas. *PLoS One*
763 **10**, e0121314, doi:10.1371/journal.pone.0121314 (2015).
764 65 Browaeys, R., Saelens, W. & Saeys, Y. NicheNet: modeling intercellular communication by
765 linking ligands to target genes. *Nat Methods* **17**, 159-162, doi:10.1038/s41592-019-0667-
766 5 (2020).
767 66 Kang, J. B. *et al.* Efficient and precise single-cell reference atlas mapping with Symphony.
768 *Nat Commun* **12**, 5890, doi:10.1038/s41467-021-25957-x (2021).
769 67 Yasumizu, Y. *et al.* Myasthenia gravis-specific aberrant neuromuscular gene expression by
770 medullary thymic epithelial cells in thymoma. *Nat Commun* **13**, 4230,
771 doi:10.1038/s41467-022-31951-8 (2022).
772
773

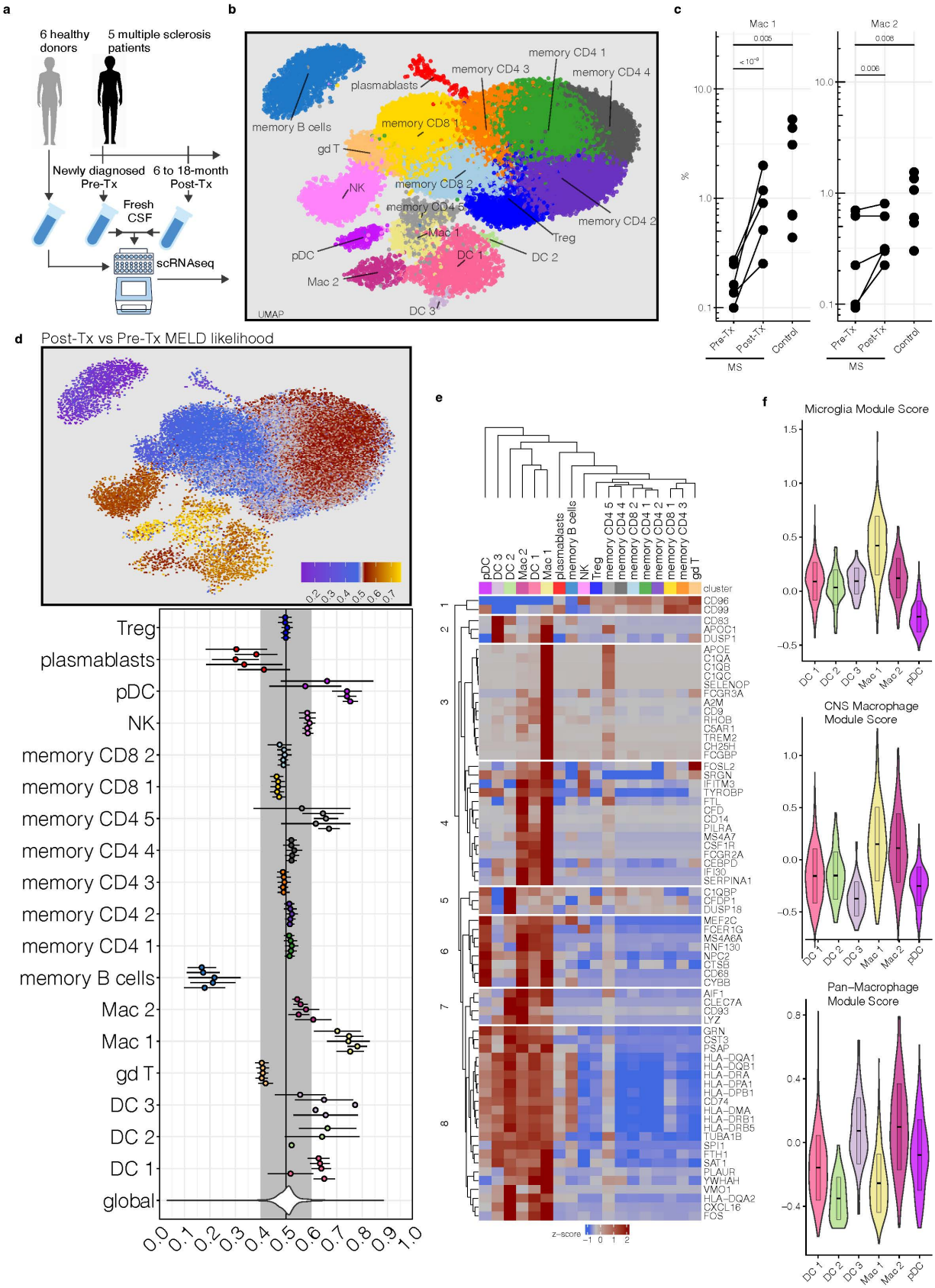
a
6 healthy donors
5 multiple sclerosis patients
Newly diagnosed Pre-Tx
6 to 18-month Post-Tx
Fresh CSF
scRNAseq
b
memory CD4 1
memory CD4 3
memory CD4 4
plasmablasts
memory B cells
memory CD8 1
gd T
NK
memory CD8 2
memory CD4 5
Mac 1
memory CD4 2
Treg
pDC
DC 1
DC 2
Mac 2
DC 3
UMAP
c
Mac 1
Mac 2
0.005
0.006
%
Pre-Tx
Post-Tx
Control
MS
d
Post-Tx vs Pre-Tx MELD likelihood
Treg
plasmablasts
pDC
NK
memory CD8 2
memory CD8 1
memory CD4 5
memory CD4 4
memory CD4 3
memory CD4 2
memory CD4 1
memory B cells
Mac 2
Mac 1
gd T
DC 3
DC 2
DC 1
global
e
cluster
z-score
f
Microglia Module Score
CNS Macrophage Module Score
Pan-Macrophage Module Score
DC 1
DC 2
DC 3
Mac 1
Mac 2
pDC

774

775 **Fig 1: Microglia-like CSF macrophages increase in frequency in MS patients post- B cell**
776 **depletion therapy**. **a,** Healthy donor and MS patient sample collection scheme for scRNAseq
777 analysis (n = 6 healthy donors, n= 5 MS patients pre-treatment, n= 5 matched MS patients post-
778 treatment). **b,** UMAP dimensionality reduction plot of immune cell clusters detected in CSF of
779 healthy donor and MS patients (n= 60,704 single cells, 17 immune cell clusters). **c,** CSF
780 macrophage cluster frequency pre- and post- B cell depletion therapy across all five MS patients.
781 **d,** MELD likelihood enrichment heatmap and patient level summary values (mean+/- SEM, n= 5
782 MS patients) post- B cell depletion therapy of all immune clusters in the CSF. **e,** Heatmap of
783 myeloid-related genes, showing average expression across all immune cell types. **f,** All myeloid
784 clusters in the CSF scored against microglia, CNS macrophage, and pan- macrophage gene
785 modules.
786
787

788

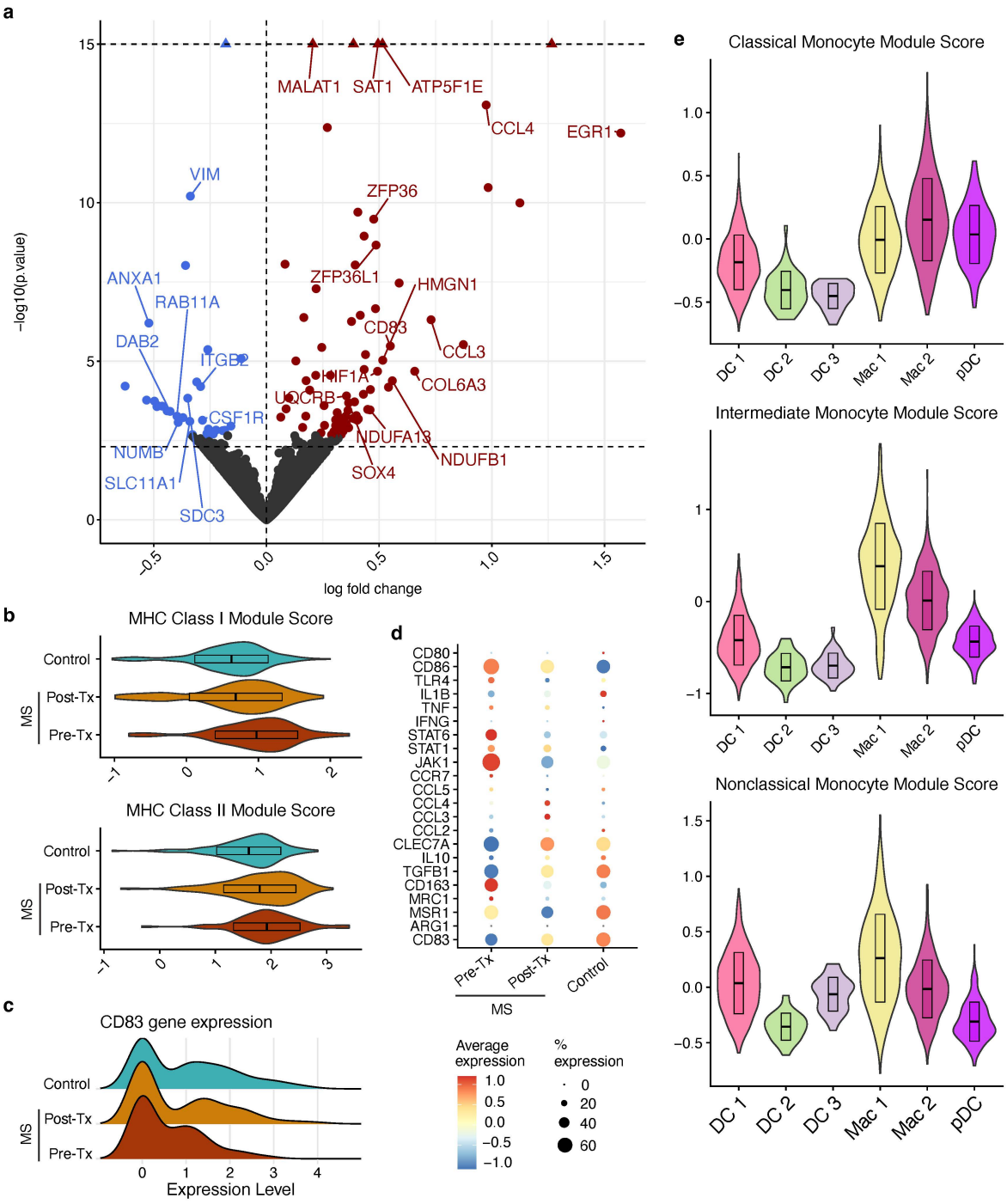
a
MALAT1
SAT1
ATP5F1E
CCL4
EGR1
VIM
ZFP36
ZFP36L1
HMGN1
ANXA1
RAB11A
CD83
DAB2
ITGB2
CCL3
HIF1A
COL6A3
UQCRB
CSF1R
NDUFA13
NUMB
NDUFB1
SOX4
SLC11A1
SDC3
−log10(p.value)
log fold change
b
MHC Class I Module Score
Control
Post-Tx
Pre-Tx
MS
MHC Class II Module Score
c
CD83 gene expression
Expression Level
d
CD80
CD86
TLR4
IL1B
TNF
IFNG
STAT6
STAT1
JAK1
CCR7
CCL5
CCL4
CCL3
CCL2
CLEC7A
IL10
TGFB1
CD163
MRC1
MSR1
ARG1
CD83
Average expression
% expression
e
Classical Monocyte Module Score
Intermediate Monocyte Module Score
Nonclassical Monocyte Module Score
DC 1
DC 2
DC 3
Mac 1
Mac 2
pDC

789

790 **Fig 2: Enriched CSF macrophages present anti-inflammatory phenotype in MS patients**
791 **post- B cell depletion therapy**. Gene expression analyses of CSF macrophages were performed
792 by comparing cells from healthy donors (n=6) and pre- and post- B cell depletion therapy MS
793 patient samples (n=5). **a,** Volcano plot depicting differentially expressed genes in the Mac 1
794 cluster from MS patients pre- and post- B cell depletion. Blue: downregulated post-treatment, red:
795 upregulated post-treatment. -log10(p value) > 15 are capped to facilitate visualization (depicted
796 as triangles). **b,** MHC class I and class II gene module scores of healthy donor, MS pre-treatment,
797 and MS post-treatment Mac 1 cells. **c,** CD83 expression of healthy donor and MS patient Mac 1
798 cells. **d,** Dot plot depicting myeloid inflammatory and anti-inflammatory gene expression in healthy
799 donors and MS patients pre- and post- treatment. **e,** Gene module scores of all CSF myeloid
800 clusters against peripheral monocyte gene signatures. Top: classical monocyte module score,
801 middle: intermediate monocyte module score, bottom: nonclassical monocyte module score.
802

803

804

805

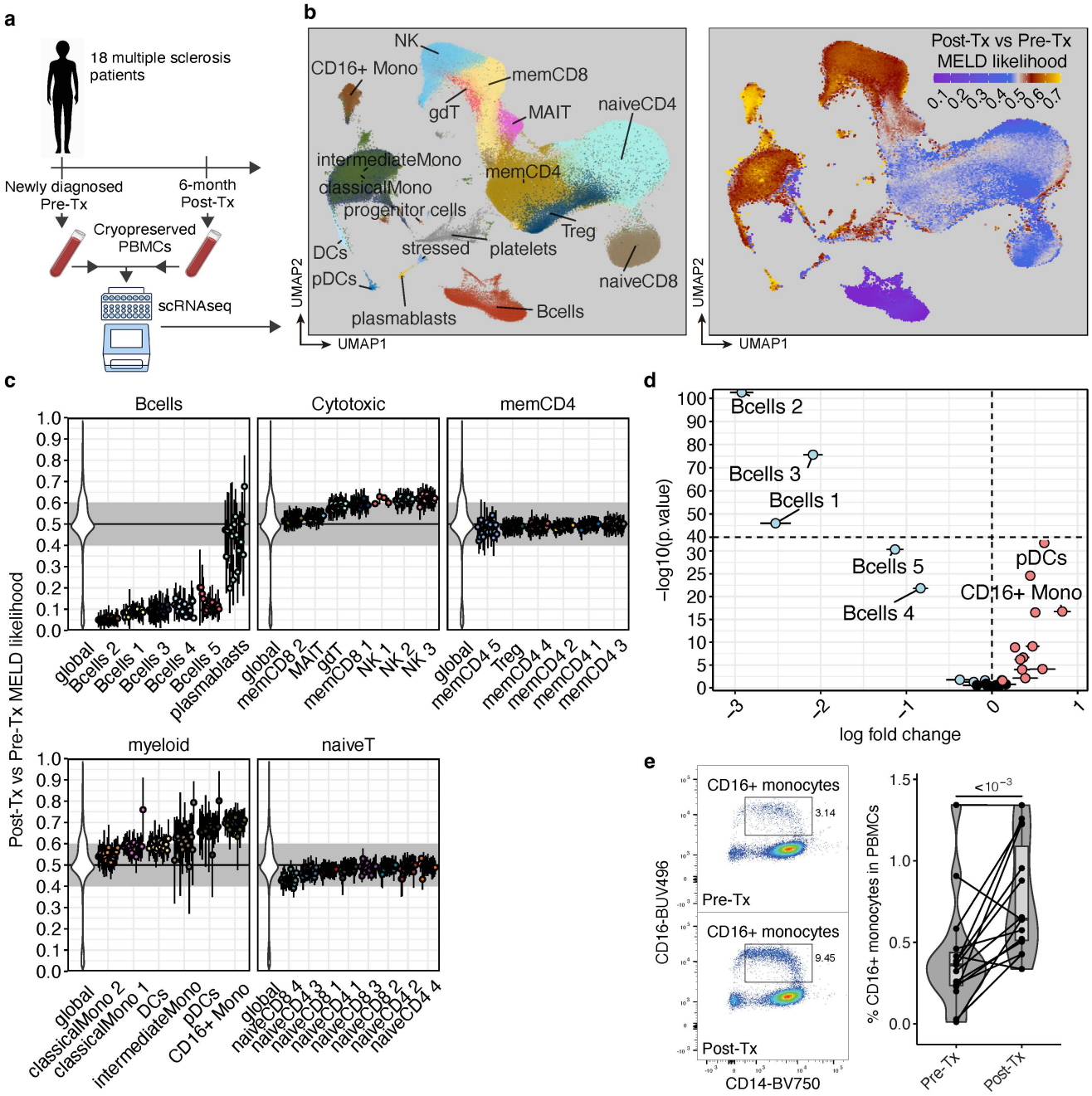
a
18 multiple sclerosis patients
Newly diagnosed Pre-Tx
6-month Post-Tx
Cryopreserved PBMCs
scRNAseq
b
NK
CD16+ Mono
memCD8
gdT
MAIT
naiveCD4
intermediateMono
memCD4
classicalMono
progenitor cells
Treg
DCs
stressed
platelets
pDCs
naiveCD8
plasmablasts
Bcells
UMAP1
UMAP2
Post-Tx vs Pre-Tx MELD likelihood
0.1 0.2 0.3 0.4 0.5 0.6 0.7
c
Bcells
Cytotoxic
memCD4
myeloid
naiveT
Post-Tx vs Pre-Tx MELD likelihood
d
Bcells 2
Bcells 3
Bcells 1
Bcells 5
Bcells 4
pDCs
CD16+ Mono
−log10(p.value)
log fold change
e
CD16+ monocytes
3.14
Pre-Tx
9.45
Post-Tx
CD16-BUV496
CD14-BV750
% CD16+ monocytes in PBMCs
<10^−3
Pre-Tx
Post-Tx

806 **Fig 3: Increased CD16$^+$ monocytes abundance after anti-CD20 treatment. a,** experimental
807 design of pre- and post-treatment (anti-CD20) PBMC samples from MS patients (n=18) for
808 droplet-based scRNAseq using 10x genomics platform. **b,** UMAP of annotated cell types (left)
809 and overlayed MELD likelihoods for post-treatment status (right). **c,** MELD likelihood patient level
810 summary values (mean+/- SEM) per fine-grained clusters and main cell types. **d,** fine-grained
811 community frequency changes post-treatment (log fold change mean estimate +/-SE from beta
812 regression, see methods). **E,** Flow cytometry validation of CD16$^+$ monocyte frequency changes
813 in MS patients PBMCs.
814
815
816
817
818
819
820
821
822
823
824
825
826
827
828
829
830
831
832
833
834
835

836

837

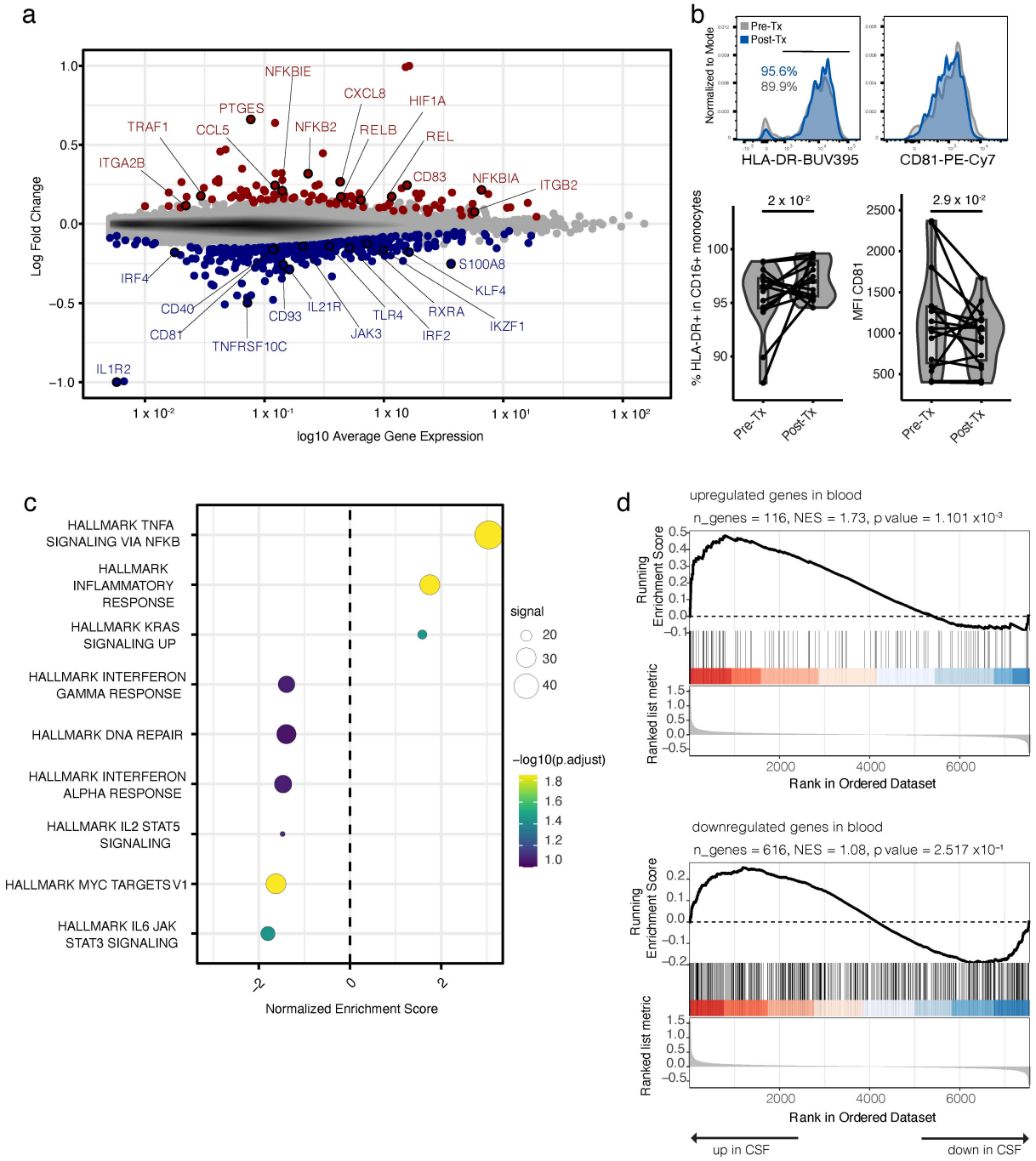
a
Log Fold Change
log10 Average Gene Expression
NFKBIE
CXCL8
HIF1A
PTGES
TRAF1
CCL5
NFKB2
RELB
REL
ITGA2B
CD83
NFKBIA
ITGB2
S100A8
IRF4
KLF4
CD40
CD93
IL21R
TLR4
RXRA
IKZF1
CD81
JAK3
IRF2
TNFRSF10C
IL1R2
b
Pre-Tx
Post-Tx
95.6%
89.9%
Normalized to Mode
HLA-DR-BUV395
CD81-PE-Cy7
2 x 10-2
2.9 x 10-2
% HLA-DR+ in CD16+ monocytes
MFI CD81
Pre-Tx
Post-Tx
c
HALLMARK TNFA SIGNALING VIA NFKB
HALLMARK INFLAMMATORY RESPONSE
HALLMARK KRAS SIGNALING UP
HALLMARK INTERFERON GAMMA RESPONSE
HALLMARK DNA REPAIR
HALLMARK INTERFERON ALPHA RESPONSE
HALLMARK IL2 STAT5 SIGNALING
HALLMARK MYC TARGETS V1
HALLMARK IL6 JAK STAT3 SIGNALING
Normalized Enrichment Score
signal
20
30
40
−log10(p.adjust)
1.8
1.6
1.4
1.2
1.0
d
upregulated genes in blood
n_genes = 116, NES = 1.73, p value = 1.101 x10-3
Running Enrichment Score
Ranked list metric
Rank in Ordered Dataset
downregulated genes in blood
n_genes = 616, NES = 1.08, p value = 2.517 x10-1
Running Enrichment Score
Ranked list metric
Rank in Ordered Dataset
up in CSF
down in CSF

838

Fig 4: Differential gene expression in CD16$^+$ monocyte post-treatment. A, Mean abundance (MA) plot of gene expression changes, differentially expressed genes (DGE) are highlighted in red (upregulated post-treatment), or blue (downregulated post-treatment). **B,** Flow cytometry of HLA-DR and CD81 expression in CD16$^+$ monocytes (n=16). **C,** GeneSet Enrichment Analysis (GSEA) using the Hallmark genesets in CD16$^+$ monocytes. **D,** Custom GSEA analysis of PBMC monocytes post-treatment signature genesets (up- and downregulated genes) tested on CSF macrophage Mac 1 dataset (From Fig 1).

871

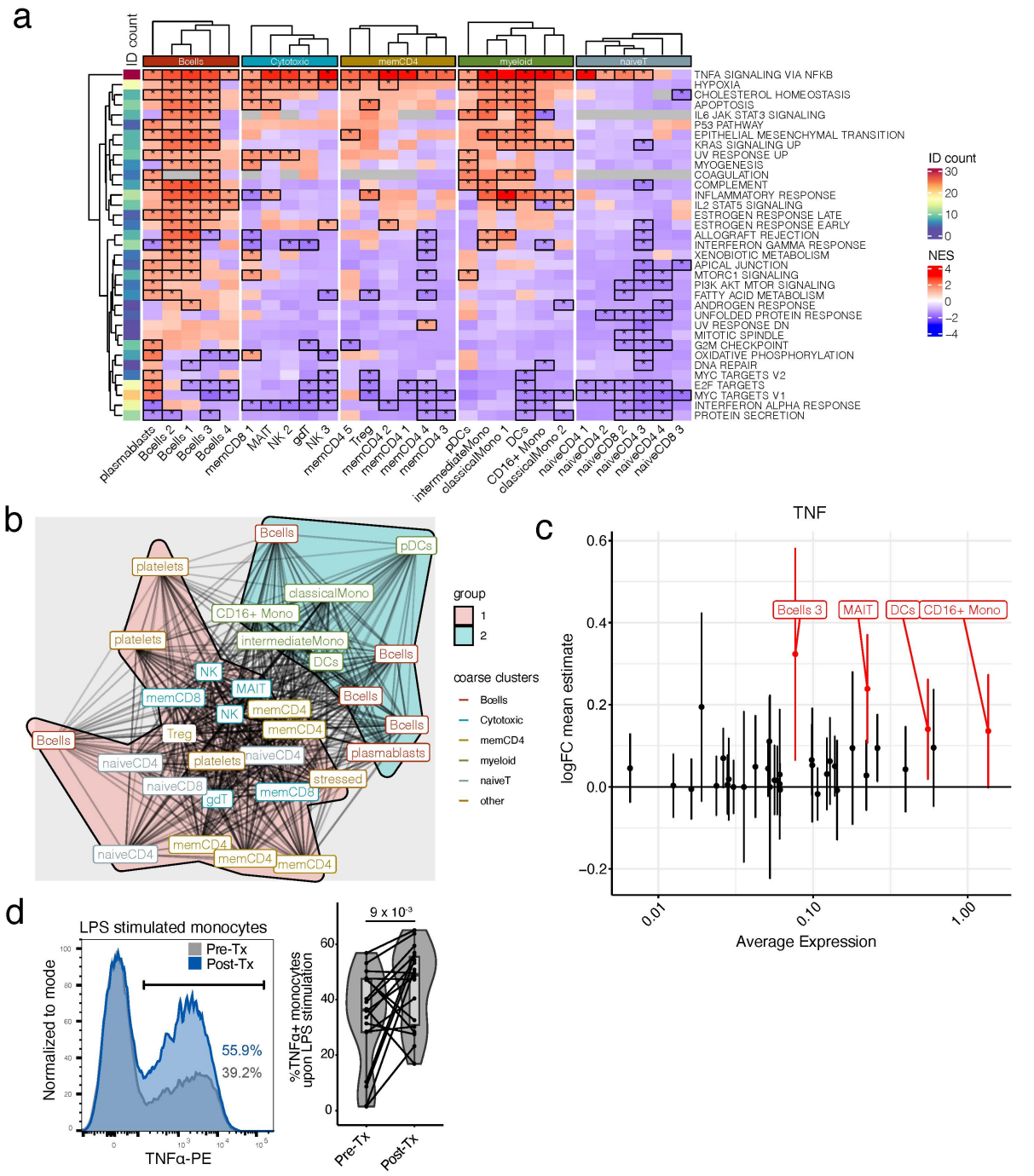
a
ID count
Bcells
Cytotoxic
memCD4
myeloid
naiveT
TNFA SIGNALING VIA NFKB
HYPOXIA
CHOLESTEROL HOMEOSTASIS
APOPTOSIS
IL6 JAK STAT3 SIGNALING
P53 PATHWAY
EPITHELIAL MESENCHYMAL TRANSITION
KRAS SIGNALING UP
UV RESPONSE UP
MYOGENESIS
COAGULATION
COMPLEMENT
INFLAMMATORY RESPONSE
IL2 STAT5 SIGNALING
ESTROGEN RESPONSE LATE
ESTROGEN RESPONSE EARLY
ALLOGRAFT REJECTION
INTERFERON GAMMA RESPONSE
XENOBIOTIC METABOLISM
APICAL JUNCTION
MTORC1 SIGNALING
PI3K AKT MTOR SIGNALING
FATTY ACID METABOLISM
ANDROGEN RESPONSE
UNFOLDED PROTEIN RESPONSE
UV RESPONSE DN
MITOTIC SPINDLE
G2M CHECKPOINT
OXIDATIVE PHOSPHORYLATION
DNA REPAIR
MYC TARGETS V2
E2F TARGETS
MYC TARGETS V1
INTERFERON ALPHA RESPONSE
PROTEIN SECRETION
plasmablasts
Bcells 2
Bcells 1
Bcells 3
Bcells 4
memCD8 1
MAIT
NK 2
gdT
NK 3
memCD4 5
Treg
memCD4 2
memCD4 1
memCD4 4
memCD4 3
pDCs
intermediateMono
classicalMono 1
DCs
CD16+ Mono
classicalMono 2
naiveCD4 1
naiveCD4 2
naiveCD8 2
naiveCD4 3
naiveCD4 4
naiveCD8 3
ID count
30
20
10
0
NES
4
2
0
−2
−4
b
Bcells
pDCs
platelets
classicalMono
CD16+ Mono
intermediateMono
DCs
NK
MAIT
memCD8
memCD4
Treg
naiveCD4
naiveCD8
gdT
plasmablasts
stressed
group
1
2
coarse clusters
Bcells
Cytotoxic
memCD4
myeloid
naiveT
other
c
TNF
Bcells 3
MAIT
DCs
CD16+ Mono
logFC mean estimate
0.6
0.4
0.2
0.0
−0.2
0.01
0.10
1.00
Average Expression
d
LPS stimulated monocytes
Pre-Tx
Post-Tx
Normalized to mode
55.9%
39.2%
TNFα-PE
9 x 10⁻³
%TNFα+ monocytes upon LPS stimulation
60
40
20
0
Pre-Tx
Post-Tx

872
873

874 **Fig 5: Geneset enrichment analysis (GSEA) of anti-CD20 gene expression alterations**
875 **across cell types. a,** Heatmap of normalized enrichment scores (NES) from post-treatment
876 GSEA analyses run for each cluster shows ubiquitous increase in TNFα-NFκB pathway.
877 Differentially enriched genesets are highlighted with a *. "ID count" depicts the number of times a
878 geneset is found enriched across communities. **b,** Overlap graph-analysis of leading edge genes
879 for the "TNFα signaling via NFκB" geneset across cell types highlights two sets of signatures: B
880 and myeloid cells vs. T cells. **c,** Pre- and post- treatment fold change of *TNFA* transcript across
881 clusters (differential expression is highlighted in red). **d,** *In vitro* validation of TNFα upregulation
882 pre- and post- B cell depletion at the protein level in MS patient monocytes (n= 18) by intracellular
883 flow cytometry staining after LPS stimulation.
884
885
886
887
888
889
890
891
892
893
894
895
896
897
898
899
900
901
902
903
904
905

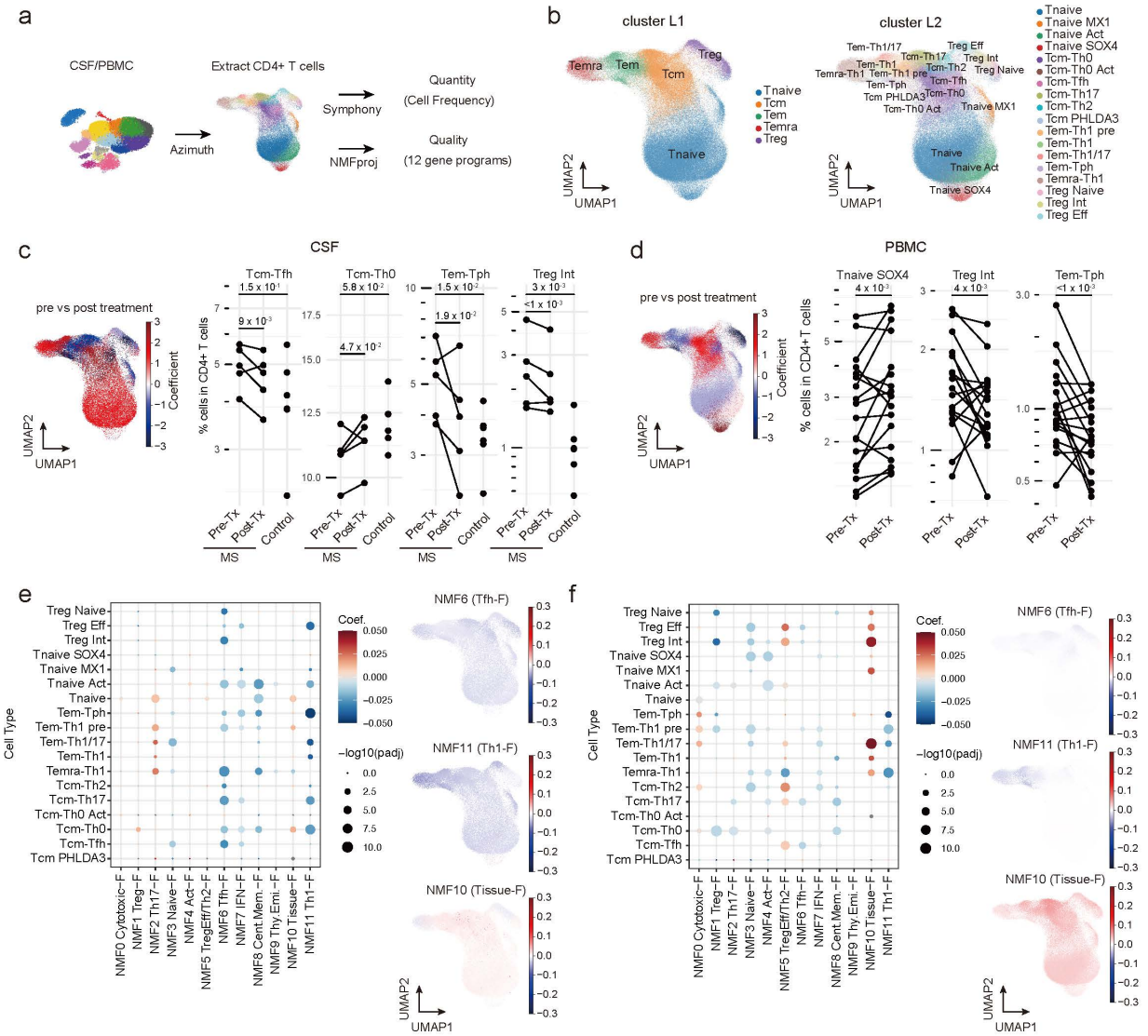
a
CSF/PBMC
Extract CD4+ T cells
Azimuth
Symphony
Quantity
(Cell Frequency)
NMFproj
Quality
(12 gene programs)
b
cluster L1
Temra
Tem
Tcm
Treg
Tnaive
UMAP2
UMAP1
cluster L2
Tem-Th1/17
Tem-Th1
Temra-Th1
Tem-Th1 pre
Tem-Tph
Tcm PHLDA3
Tcm-Th17
Tcm-Th2
Tcm-Th0
Tcm-Th0 Act
Tcm-Tfh
Treg Eff
Treg Int
Treg Naive
Tnaive MX1
Tnaive Act
Tnaive SOX4
Tnaive
Tcm
Tem
Temra
Treg
Tnaive
Tnaive MX1
Tnaive Act
Tnaive SOX4
Tcm-Th0
Tcm-Th0 Act
Tcm-Tfh
Tcm-Th17
Tcm-Th2
Tcm PHLDA3
Tem-Th1 pre
Tem-Th1
Tem-Th1/17
Tem-Tph
Temra-Th1
Treg Naive
Treg Int
Treg Eff
c
CSF
pre vs post treatment
Coefficient
% cells in CD4+ T cells
Tcm-Tfh
Tcm-Th0
Tem-Tph
Treg Int
1.5 x 10-1
9 x 10-3
5.8 x 10-2
4.7 x 10-2
1.5 x 10-2
1.9 x 10-2
3 x 10-3
<1 x 10-3
Pre-Tx
Post-Tx
Control
MS
d
PBMC
pre vs post treatment
Tnaive SOX4
Treg Int
Tem-Tph
4 x 10-3
4 x 10-3
<1 x 10-3
e
Cell Type
Treg Naive
Treg Eff
Treg Int
Tnaive SOX4
Tnaive MX1
Tnaive Act
Tnaive
Tem-Tph
Tem-Th1 pre
Tem-Th1/17
Tem-Th1
Temra-Th1
Tcm-Th2
Tcm-Th17
Tcm-Th0 Act
Tcm-Th0
Tcm-Tfh
Tcm PHLDA3
NMF0 Cytotoxic−F
NMF1 Treg−F
NMF2 Th17−F
NMF3 Naive−F
NMF4 Act−F
NMF5 TregEff/Th2−F
NMF6 Tfh−F
NMF7 IFN−F
NMF8 Cent.Mem.−F
NMF9 Thy.Emi.−F
NMF10 Tissue−F
NMF11 Th1−F
Coef.
−log10(padj)
NMF6 (Tfh-F)
NMF11 (Th1-F)
NMF10 (Tissue-F)
UMAP2
UMAP1
f

Fig 6: Detailed Analysis of CD4$^+$ T Cell Alterations Following Anti-CD20 Treatment. a, Schematic illustration of the analysis of CD4$^+$ T cells using a reference mapping and NMFproj. From CSF and PBMC samples, CD4$^+$ T cells were extracted using Azimuth, and detailed CD4$^+$ T clusters were predicted using Symphony. The 12 gene programs were calculated using NMFproj. **b,** Inferred CD4$^+$ T cell clusters on UMAP plot. The clusters were assigned to either a major cluster (L1) or a detailed cluster (L2) level. **c, d,** Cell frequency changes after anti-CD20 treatment in CSF **(c)** and PBMC **(d)**. Coefficients of cell frequency change per cluster L2 quantified GLM (method) are visualized on the UMAP plot (left). The populations with cell frequency increases post-B cell depletion treatment are shown in red. CD4$^+$ T cluster frequency pre- and post-B cell depletion therapy (right). Significantly altered clusters are shown. See Supplementary Figure 8c and 9c for additional details. **e, f,** Alterations of gene programs extracted by NMFproj after anti-CD20 treatment in CSF **(e)** and PBMC **(f)**. Dot plots depicting NMF cell feature changes in each cell type (left). Dot colors show coefficients, and sizes show the significance of GLM (method). The coefficient of gene program change per cluster for some gene programs was shown on UMAP plots (right). Annotations and representative genes of gene programs are following; NMF0 (Cytotoxic-Feature or Cytotoxic-F; *GZMB*, *CX3CR1*), NMF1 (Treg-F; *FOXP3*, *IL2RA*), NMF2 (Th17-F; *RORC*, *CCR6*), NMF3 (Naive-F; *CCR7*, *BACH2*), NMF4 (Activation-F or Act-F; *DACT1*, *CDK6*), NMF5 (TregEff/Th2-F; *HLA-DR*s, *CCR10*), NMF6 (Tfh-F; *MAF*, *CXCR5*), NMF7 (Interferon-F or IFN-F; *OAS1*, *MX1*), NMF8 (Central Memory-F; *CRIP2*, *PLP2*), NMF9 (Thymic Emigrant-F; *SOX4*, *PECAM1*), NMF10 (Tissue-F; *JUNB*, *NFKBIA*) NMF11 (Th1-F; *GZMK*, *EOMES*)

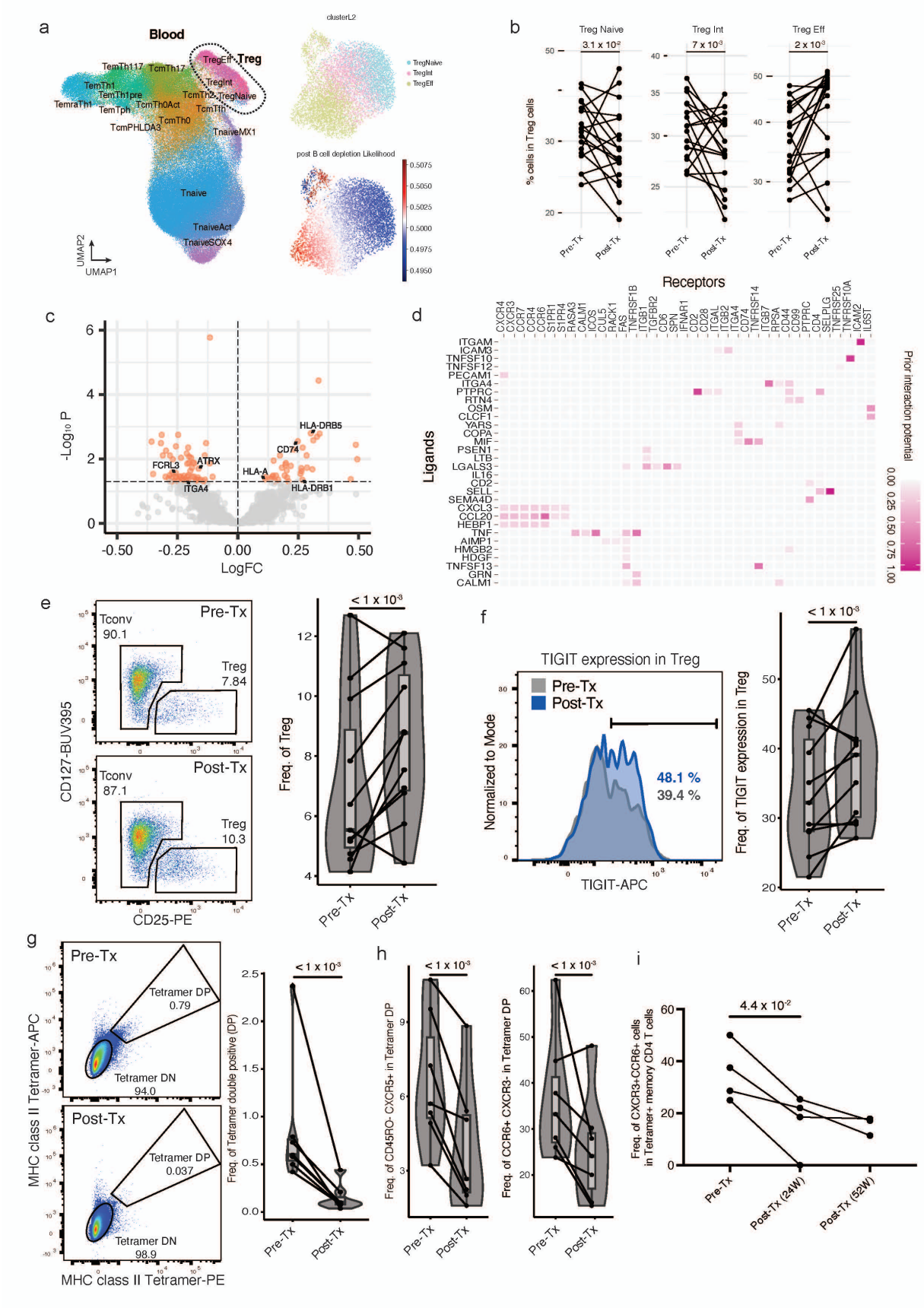
a
Blood
clusterL2
TregNaive
TregInt
TregEff
post B cell depletion Likelihood
UMAP2
UMAP1
b
Treg Naive
Treg Int
Treg Eff
% cells in Treg cells
Pre-Tx
Post-Tx
c
-Log10 P
LogFC
HLA-DRB5
CD74
FCRL3
ATRX
HLA-A
ITGA4
HLA-DRB1
d
Receptors
Ligands
Prior interaction potential
e
Pre-Tx
Post-Tx
Tconv
Treg
CD127-BUV395
CD25-PE
Freq. of Treg
f
TIGIT expression in Treg
Normalized to Mode
TIGIT-APC
48.1 %
39.4 %
Freq. of TIGIT expression in Treg
g
Tetramer DP
Tetramer DN
MHC class II Tetramer-APC
MHC class II Tetramer-PE
Freq. of Tetramer double positive (DP)
h
Freq. of CD45RO- CXCR5+ in Tetramer DP
Freq. of CCR6+ CXCR3- in Tetramer DP
i
Freq. of CXCR3+CCR6+ cells in Tetramer+ memory CD4 T cells
Post-Tx (24W)
Post-Tx (52W)

937

938 **Fig 7: B cell depletion induces an increase in TIGIT$^+$ Tregs and reduces autoreactive T**
939 **cells. a,** Visualization of Treg population extraction and changes after B cell depletion treatment.
940 Predicted CD4$^+$ T clusters and Tregs (dotted line) on UMAP plot (left). Re-embedding of extracted
941 Tregs using UMAP (top right). B cell depletion treatment associated relative likelihood in Treg
942 populations calculated using MELD (bottom right). **b,** Frequency changes of each subpopulation
943 within the Treg group. **c,** Volcano plot depicting differentially expressed genes in Tregs,
944 particularly highlighting genes encoding surface proteins. **d,** Heatmap displaying predicted
945 interactions between myeloid cell-derived ligands (limited to genes differentially regulated with B
946 cell depletion treatment) and Treg-derived receptors, weighted by prior interaction potential. **e,f,**
947 Flow cytometry data of Tregs frequency **(e)** and TIGIT protein expression of Tregs **(f)** in MS patient
948 PBMC (n=11) after B cell depletion treatment, **g,** Flow cytometry analysis of myelin tetramer-
949 reactive CD4$^+$ T cell frequency at pre-treatment and 6-month post-treatment timepoints (n=7). **h,**
950 Tfh (CD45RA$^-$CXCR5$^+$) cells in tetramer-reactive CD4$^+$ T cells and Th17 (CCR6$^+$CXCR3$^-$) cells in
951 tetramer-reactive CD4$^+$ T cells frequencies at pre-treatment and 6-month post-treatment
952 timepoints (n=7). **i.** Longitudinal kinetic analysis of the frequency of autoreactive CCR6$^+$CXCR3$^+$
953 CD4$^+$ T cells using flow cytometry at pre-treatment (n=4), 24-week post-treatment (n=4) and 52
954 week post-treatment (n=3) timepoints.
955